The 2dF galaxy redshift survey: near-infrared galaxy luminosity functions

Shaun Cole,[1]★ Peder Norberg,[1] Carlton M. Baugh,[1] Carlos S. Frenk,[1]
Joss Bland-Hawthorn,[2] Terry Bridges,[2] Russell Cannon,[2] Matthew Colless,[3] Chris Collins,[4]
Warrick Couch,[5] Nicholas Cross,[6] Gavin Dalton,[7] Roberto De Propris,[5] Simon P. Driver,[6]
George Efstathiou,[8] Richard S. Ellis,[9] Karl Glazebrook,[10] Carole Jackson,[3] Ofer Lahav,[8]
Ian Lewis,[2] Stuart Lumsden,[11] Steve Maddox,[12] Darren Madgwick,[8] John A. Peacock,[13]
Bruce A. Peterson,[3] Will Sutherland[13] and Keith Taylor[2] (The 2dFGRS Team)

[1]*Department of Physics, University of Durham, Science Laboratories, South Road, Durham DH1 3LE*
[2]*Anglo-Australian Observatory, PO Box 296, Epping, NSW 2121, Australia*
[3]*Research School of Astronomy & Astrophysics, The Australian National University, Weston Creek, ACT 2611, Australia*
[4]*Astrophysics Research Institute, Liverpool John Moores University, Twelve Quays House, Egerton Wharf, Birkenhead, L14 1LD*
[5]*Department of Astrophysics, University of New South Wales, Sydney, NSW2052, Australia*
[6]*School of Physics and Astronomy, North Haugh, St Andrews, Fife, KY16 9SS*
[7]*Department of Physics, Keble Road, Oxford OX1 3RH*
[8]*Institute of Astronomy, University of Cambridge, Madingley Road, Cambridge CB3 0HA*
[9]*Department of Astronomy, California Institute of Technology, Pasadena, CA 91125, USA*
[10]*Department of Physics & Astronomy, Johns Hopkins University, 3400 North Charles Street Baltimore, MD 212182686, USA*
[11]*Department of Physics & Astronomy, E C Stoner Building, Leeds LS2 9JT*
[12]*School of Physics and Astronomy, University of Nottingham, University Park, Nottingham, NG7 2RD*
[13]*Institute of Astronomy, University of Edinburgh, Royal Observatory, Edinburgh EH9 3HJ*

ABSTRACT

We combine the Two Micron All Sky Survey (2MASS) Extended Source Catalogue and the 2dF Galaxy Redshift Survey to produce an infrared selected galaxy catalogue with 17 173 measured redshifts. We use this extensive data set to estimate the galaxy luminosity functions in the J- and K_S-bands. The luminosity functions are fairly well fitted by Schechter functions with parameters $M_J^* - 5\log h = -22.36 \pm 0.02$, $\alpha_J = -0.93 \pm 0.04$, $\Phi_J^* = 0.0104 \pm 0.0016\,h^3\,{\rm Mpc}^{-3}$ in the J-band and $M_{K_S}^* - 5\log h = -23.44 \pm 0.03$, $\alpha_{K_S} = -0.96 \pm 0.05$, $\Phi_{K_S}^* = 0.0108 \pm 0.0016\,h^3\,{\rm Mpc}^{-3}$ in the K_S-band (2MASS Kron magnitudes). These parameters are derived assuming a cosmological model with $\Omega_0 = 0.3$ and $\Lambda_0 = 0.7$. With data sets of this size, systematic rather than random errors are the dominant source of uncertainty in the determination of the luminosity function. We carry out a careful investigation of possible systematic effects in our data. The surface brightness distribution of the sample shows no evidence that significant numbers of low surface brightness or compact galaxies are missed by the survey. We estimate the present-day distributions of $b_J - K_S$ and $J - K_S$ colours as a function of the absolute magnitude and use models of the galaxy stellar populations, constrained by the observed optical and infrared colours, to infer the galaxy stellar mass function. Integrated over all galaxy masses, this yields a total mass fraction in stars (in units of the critical mass density) of $\Omega_{\rm stars}h = (1.6 \pm 0.24) \times 10^{-3}$ for a Kennicutt initial mass function (IMF) and $\Omega_{\rm stars}h = (2.9 \pm 0.43) \times 10^{-3}$ for a Salpeter IMF. These values are consistent with those inferred from observational estimates of the total star formation history of the Universe provided that dust extinction corrections are modest.

Key words: surveys – galaxies: luminosity function, mass function – infrared: galaxies.

★E-mail: Shaun.Cole@durham.ac.uk

1 INTRODUCTION

The near-infrared galaxy luminosity function is an important characteristic of the local galaxy population. It is a much better tracer of evolved stars, and hence of the total stellar content of galaxies, than optical luminosity functions which can be dominated by young stellar populations and are also strongly affected by dust extinction. Hence, infrared luminosities can be much more directly related to the underlying stellar mass of galaxies and so knowledge of the present form and evolution of the infrared galaxy luminosity function places strong constraints on the history of star formation in the Universe and on galaxy formation models (e.g. Cole et al. (2000) and references therein).

The local *K*-band luminosity function has been estimated from optically selected samples by Mobasher, Sharples & Ellis (1993), Szokoly et al. (1998) and Loveday (2000) and from *K*-band surveys by Glazebrook et al. (1995) and Gardner et al. (1997). The existing *K*-band surveys are small. The largest, by Gardner et al., covers only $4 \deg^2$ and contains only 510 galaxies. The recent survey of Loveday covers a much larger solid angle. In this survey the redshifts were known in advance of measuring the *K*-band magnitudes, and this was exploited by targetting bright and faint galaxies resulting in an effective sample size much larger than the 345 galaxies actually measured. However, like all optically selected samples, it suffers from the potential problem that galaxies with extremely red infrared to optical colours could be missed. In this paper we combine the Two Micron All Sky Survey (2MASS) and the 2dF Galaxy Redshift Survey (2dFGRS) to create an infrared selected redshift survey subtending $2151.6 \deg^2$. Currently the sky coverage of both surveys is incomplete, but already the overlap has an effective area of $619 \deg^2$. Within this area the redshift survey is complete to the magnitude limit of the 2MASS catalogue and so constitutes a complete survey which is 50 times larger than the previous largest published infrared selected redshift survey. A new catalogue of a similarly large area, also based on 2MASS, has very recently been analysed by Kochanek et al. (2001). They adopt isophotal rather than total magnitudes and concentrate on the dependence of the luminosity function on galaxy morphology.

In Section 2.1 we briefly describe the relevant properties of the 2dFGRS and 2MASS catalogues. Section 2.2 is a detailed examination of the degree to which the matched 2MASS–2dFGRS galaxies are a complete and representative subset of the 2MASS catalogue. Section 2.3 examines the calibration of the 2MASS total magnitudes and Section 2.4 demonstrates that the 2MASS catalogue and the inferred luminosity functions are not affected by surface brightness selection effects. In Section 3 we present the method by which we compute *k*-corrections and evolutionary corrections and relate the observed luminosities to the underlying stellar mass. The estimation methods and normalization of the luminosity functions are described briefly in Section 4. Our main results are presented and discussed in Section 5. These include estimates of the *J* and K_S (*K*-short) luminosity functions, the $b_J - K_S$ and $J - K_S$ colour distributions as a function of absolute magnitude and the distribution of spectral type. We also estimate the stellar mass function of galaxies, which can be integrated to infer the fraction of baryons in the Universe which are in the form of stars. We conclude in Section 6.

2 THE DATA SET

The data that we analyse are the Extended Source Catalogue from the second incremental release of the 2MASS (http://pegasus. phast.umass.edu) and the galaxy catalogue of the 2dFGRS (http:// www.mso.anu.edu.au/2dFGRS). Here, we present the relevant properties of these two catalogues and investigate their selection characteristics and level of completeness.

2.1 Selection criteria

The 2MASS is a ground-based, all-sky imaging survey in the *J*, *H* and K_S bands. Details of how extended sources are identified and their photometric properties measured are given by Jarrett et al. (2000). The detection sensitivity (10σ) for extended sources is quoted as 14.7, 13.9 and 13.1 mag in *J*, *H* and K_S, respectively. The complete survey is expected to contain one million galaxies of which approximately 580 000 are contained in the second incremental data release made public in 2000 March.

The 2dFGRS is selected in the photographic b_J band from the automated plate measurement (APM) Galaxy Survey (Maddox et al. 1990a,b, 1996) and subsequent extensions to it, that include a region in the Northern Galactic cap (Maddox et al., in preparation). The survey covers approximately $2151.6 \deg^2$ consisting of two broad declination strips. The larger is centred on the Southern Galactic Pole (SGP) and approximately covers $-22°.5 > \delta > -37°.5$, $21^h40^m < \alpha < 3^h30^m$; the smaller strip is in the Northern Galactic cap and covers $2°.5 > \delta > -7°.5$, $9^h50^m < \alpha < 14^h50^m$. In addition, there are a number of randomly located circular two-degree fields scattered across the full extent of the low extinction regions of the southern APM galaxy survey. There are some gaps in the 2dFGRS sky coverage within these boundaries as a result of small regions that have been excluded around bright stars and satellite trails. The 2dFGRS aims to measure the redshifts of all the galaxies within these boundaries with extinction-corrected b_J magnitudes brighter than 19.45. When complete, at the end of 2001, 250 000 galaxy redshifts would have been measured. In this paper we use the 140 000 redshifts obtained prior to 2000 September.

The overlap of the two surveys is very good. There are some gaps in the sky coverage because of strips of the sky that were not included in the 2MASS second incremental release, but overall a substantial fraction of the $2151.6 \deg^2$ of the 2dFGRS is covered by 2MASS. The homogeneity and extensive sky coverage of the combined data set make it ideal for studies of the statistical properties of the galaxy population.

2.2 The completeness of the matched 2Mass–2dFGRS catalogue

Here we consider whether all the 2MASS galaxies within the 2dFGRS survey region have 2dFGRS counterparts and assess the extent to which the fraction of galaxies with measured redshifts represents an unbiased subsample.

The astrometry in both 2MASS and 2dFGRS is, in general, very good and it is an easy matter to match objects in the two catalogues. We choose to find the closest pairs within a search radius equal to three quarters of the semimajor axis of the *J*-band image (denoted j_r_e in the 2MASS data base). Scaling the search radius in this way helps with the matching of large extended objects. This procedure results in the identification of 2dFGRS counterparts for 40 121 of the 2MASS objects, when at random one would only expect to find a handful of such close pairs. Moreover, the distribution of separations shown in Fig. 1 peaks at 0.5 arcsec, with only 3 per cent having separations greater than 3 arcsec. A
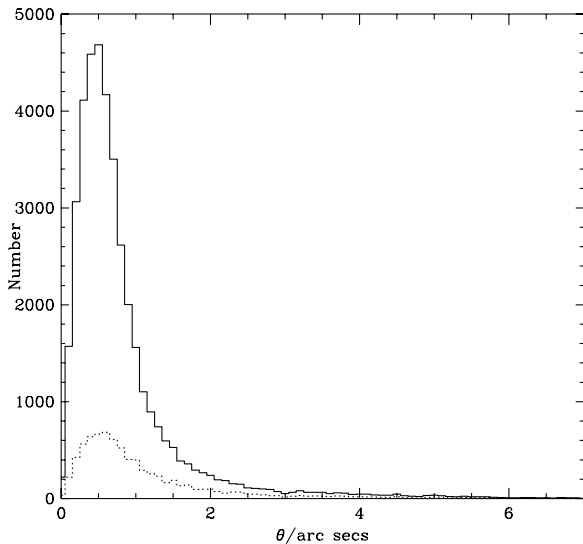
Figure 1. The distribution of angular separation, θ, for matched 2MASS–2dFGRS galaxies. The solid histogram is the distribution for the whole catalogue, and the dotted histogram for the subset of 2MASS galaxies with semimajor axes larger than 12 arcsec.

significant part of this tail comes from the most extended objects as is evident from the dotted histogram in Fig. 1 which shows objects with semimajor axes larger than 12 arcsec. Thus, we can be very confident in these identifications.

The 40 121 2MASS objects for which we have found secure 2dFGRS counterparts amount to 88.6 per cent of the 2MASS extended sources that fall within the boundary of the 2dFGRS. As discussed below, a more restrictive criterion that includes only sources fainter than $J = 12$ that are confidently classified as galaxies by 2MASS, increases the fraction with 2dFGRS matches to 90.7 per cent. The remaining 9.3 per cent are missed for well understood reasons (star–galaxy classification: 4.6 per cent; merged or close images: 4.4 per cent; miscellaneous: 0.27 per cent), none of which ought to introduce a bias. This is confirmed explicitly, in the middle row of Fig. 2, by the close correspondence between the photometric properties of the missed 9.3 per cent and those of the larger matched sample. Hence, in estimating luminosity functions no significant bias will be introduced by assuming the matched sample to be representative of the full population. Furthermore, the distribution shown in the bottom row of Fig. 2 shows that the subset of 17 173 galaxies for which we have measured redshifts is a random sample of the full matched 2MASS–2dFGRS catalogue. This summary is the result of a thorough investigation, which we describe in the remainder of this section, into the reasons of why 11.4 per cent of the 2MASS sources are missed and whether their omission introduces a bias in the properties of the matched sample.

We first consider objects in the 2MASS catalogue which based on their images and colours are not confidently classified as galaxies. In the 2MASS data base a high e_score or g_score indicates a high probability that the object is either not an extended source or not a galaxy. A cc_flag $\neq 0$ indicates an artefact or contaminated and/or confused source. For detailed definitions of these parameters we refer the reader to Jarrett et al. (2000). Rejecting all objects which have either e_score > 1.4, g_score > 1.4 or cc_flag $\neq 0$ removes just 6.7 per cent of the total. However, removing these reduces significantly the fraction of the 2MASS sample that does not match with the 2dFGRS

catalogue from 11.4 to 9.6 per cent. Thus, it is likely that about 30 per cent of the 2MASS objects which have e_score > 1.4, g_score > 1.4 or cc_flag $\neq 0$ are not galaxies.

The 2MASS may contain a tail of very red objects that are too faint in the b_J-band to be included in the $b_J < 19.45$ 2dFGRS sample. Fig. 3 shows the distribution of b_J–J colours for the matched objects with $J < 14.7$. (Here, the J-band magnitude we are using is the default magnitude denoted j_m in the 2MASS data base. In Section 2.3 we will consider the issue of what magnitude definition is most appropriate for estimating the luminosity function.) The vertical dashed line indicates the colour at which this sample begins to become incomplete because of the $b_J < 19.45$ magnitude limit of 2dFGRS. The colour distribution cuts off sharply well before this limit, suggesting that any tail of missed very red objects is extremely small. In other words the 2dFGRS is sufficiently deep that even the reddest objects detected at the faintest limits of 2MASS ought to be detected in 2dFGRS.

In the top row of Fig. 2 we compare the distributions of magnitude, colour and surface brightness for the matched and missed 2MASS objects. In general, the properties of the missed subset overlap well with those of the much larger matched subset. However, we do see that the distributions for missed objects contain tails of bright and blue objects. It is likely that this is because of the 2MASS Extended Source Catalogue being contaminated by a small population of saturated or multiple stars. The dotted histograms in the top row of Fig. 2 show the distributions of magnitude, colour and surface brightness for the bright subset of the missed objects with $J < 12$. Here we clearly see bimodal colour and surface brightness distributions. The blue peak of the colour distribution is consistent with that expected for stars (see Jarrett et al. (2000). Excluding these bright, $J < 12$, objects which are clearly contaminated by stars reduces the fraction of missed 2MASS objects from 9.6 to 9.3 per cent. The magnitude, colour and surface brightness distributions for this remaining 9.3 per cent are shown in the middle panel of Fig. 2. We see that the missed objects are slightly underrepresented at the faintest magnitudes and also slightly bluer on average than the matched sample, while the distribution of surface brightness is almost indistinguishable for the two sets of objects. These differences are small and so will introduce no significant bias in our luminosity function estimates.

To elucidate the reasons for the remaining missed 9.3 per cent of 2MASS objects we downloaded 100 1×1 arcmin images from the STScI Digitized Sky Survey (DSS) centred on the positions of a random sample of the missed 2MASS objects. In each image we plotted a symbol to indicate the position of any of the 2dFGRS galaxies within the 1×1 arcmin field. We also plotted symbols to indicate the positions and classifications of all images identified in the APM scans from which the 2dFGRS catalogue was drawn, down to a magnitude limit of $b_J \approx 20.5$. These images are classified as galaxies, stars, merged images (galaxy + galaxy, galaxy + star or star + star) or noise. This set of plots allows us to perform a census of the reasons of why some 2MASS objects are not present in the 2dFGRS survey.

The main cause for the absence of 2MASS objects in the 2dFGRS is that the APM has classified these objects as stars. These amount to 49.5 per cent of the missed sample (4.6 per cent of the full 2MASS sample). In some cases, the DSS image shows clearly that these are stars and in others that they are galaxies. However, the majority of these objects cannot easily be classified from the DSS images. Thus, they could be galaxies that the APM has falsely classified as stars or stars that 2MASS has falsely classified as
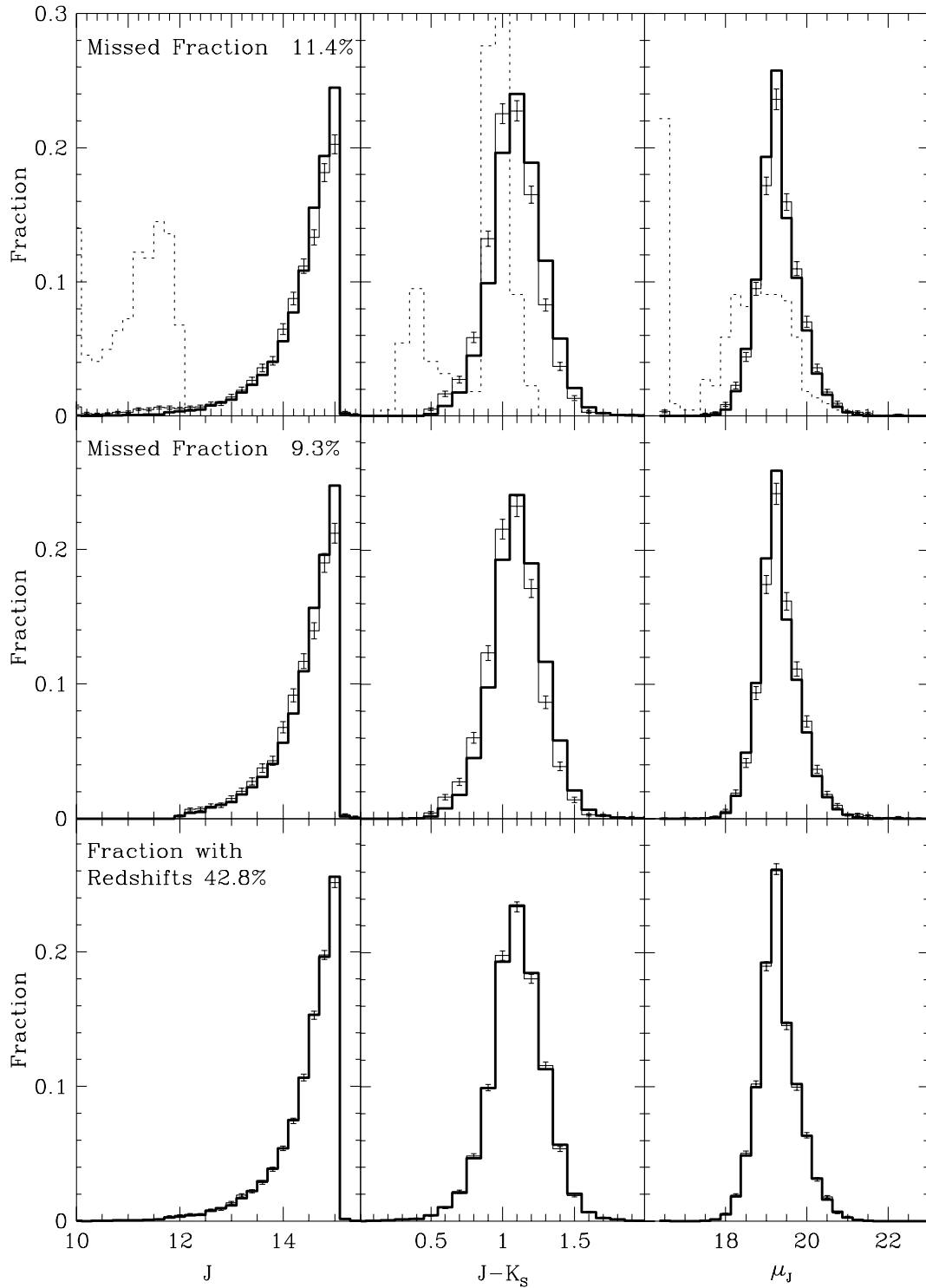
Figure 2. The distribution of the *J*-band apparent magnitude, $J - K_S$ colour and *J*-band surface brightness, μ_J, for various subsamples of the 2MASS catalogue. Here, the measure of surface brightness used is simply $\mu_J \equiv J - 5\log_{10}r$, where *J* is the Kron magnitude and *r* the Kron semimajor axis in arcsec (j_m_e and j_r_e in the 2MASS data-base). In all three rows, the thick solid histograms are the distributions for 2MASS objects that are matched with 2dFGRS galaxies. The light solid histograms in the top row are the 11.4 per cent of 2MASS galaxies that are not matched with 2dFGRS galaxies. Poisson error bars are shown on these histograms. The dashed histograms are for the bright subsample with $J < 12$. In the middle row, the light histograms show the distributions for the 9.3 per cent of 2MASS galaxies fainter than $J = 12$ and satisfying the additional image classification constraints discussed in the text that are not matched with 2dFGRS galaxies. In the bottom row, the light histograms show the distributions of the 42.8 per cent of the matched 2MASS–2dFGRS galaxies for which redshifts have been measured. The values in each histogram are the fraction of the corresponding sample that falls in each bin.
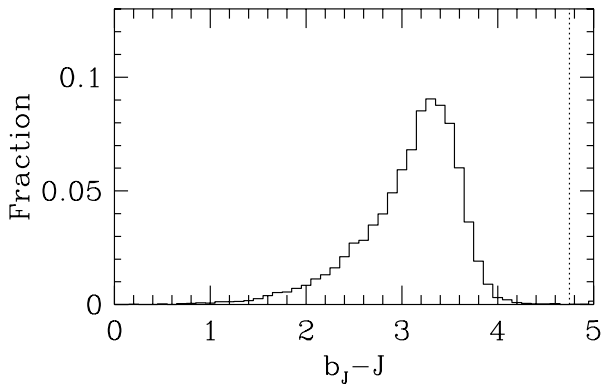
Figure 3. The solid histogram shows the distribution of b_J–J colours for 2MASS galaxies selected to have $J < 14.7$. (Here, we use the 2MASS default magnitude, denoted j_m in the 2MASS data base.) The vertical dashed line indicates the colour at which this sample begins to become incomplete because of the $b_J < 19.45$ mag limit of 2dFGRS.

galaxies. The first possibility is not unexpected since the parameters used in the APM star–galaxy separation algorithm were chosen as a compromise between high completeness and low contamination such that the expected completeness is around 95 per cent with 5 per cent stellar contamination (Maddox et al. 1990a). It is hard to rule out the possibility that this class of objects does not include a substantial fraction of stars, but if so, their presence appears not to distort the distribution of colours shown in Fig. 3. Another 47.6 per cent of the random sample (4.4 per cent of the full 2MASS sample) are classified by the APM as mergers or else consist of two close images in the DSS but are classified by the APM as a single galaxy offset from the 2MASS position. The remaining 2.9 per cent of the random sample (0.27 per cent of the full 2MASS sample) are missed for a variety of reasons including proximity to the diffraction spikes of very bright stars and poor astrometry caused by the presence of a neighbouring unclassified image.

2.3 2MASS magnitude definitions and calibration

The 2MASS extended source data base provides a large selection of different magnitude measurements. In the previous section we used the default magnitudes (denoted j_m and k_m in the 2MASS data base). These are magnitudes defined within the same circular aperture in each waveband. For galaxies brighter than $K_S = 14$, the aperture is the circular K_S-band isophote of 20 mag arcsec^{-2} and for galaxies fainter than $K_S = 14$ it is the circular J-band isophote of 21 mag arcsec^{-2}. These are not the most useful definitions of magnitude for determining the galaxy luminosity function. Since we are interested in measuring the total luminosity and ultimately the total stellar mass of each galaxy, we require a magnitude definition that better represents the total flux emitted by each galaxy. We consider Kron magnitudes (Kron 1980) and extrapolated magnitudes. Kron magnitudes (denoted j_m_e and k_m_e in the 2MASS data base) are measured within an aperture, the Kron radius, defined as 2.5 times the intensity weighted radius of the image. The extrapolated magnitudes (denoted j_m_ext and k_m_ext in the 2MASS data base) are defined by first fitting a modified exponential profile, $f(r) = f_0 \exp[-(\alpha r)^{1/\beta}]$, to the image from 10 arcsec to the 20 mag arcsec^2 isophotal radius, and extrapolating this from the Kron radius to four times this radius or 80 arcsec if this is smaller (Jarrett, private communication). Note that improvements are being made to the extended source
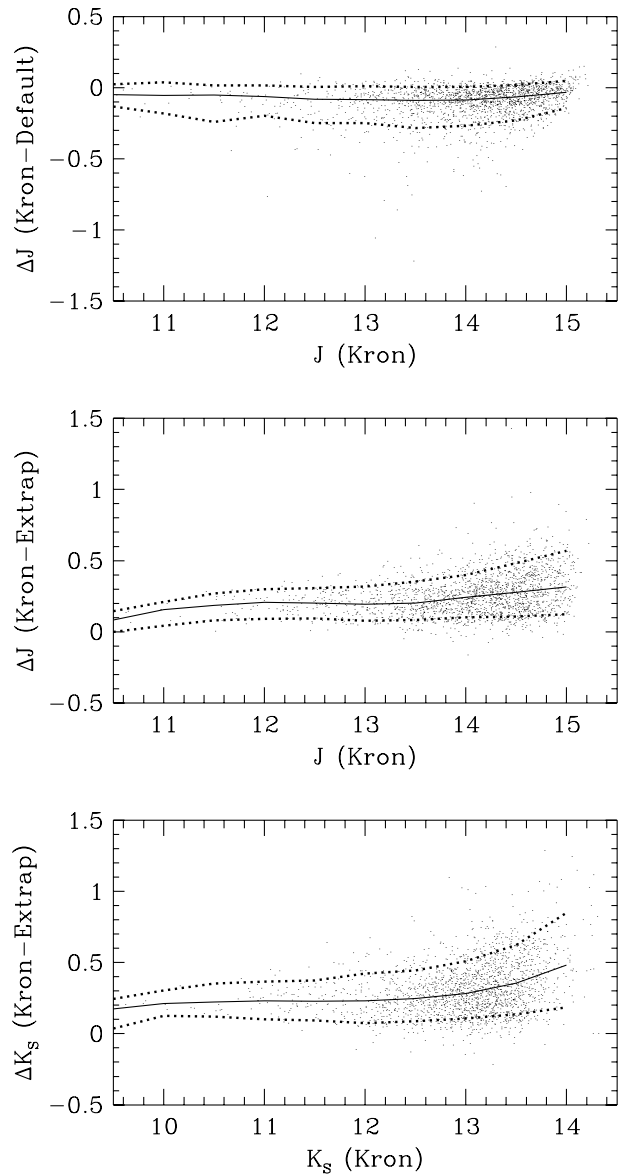

Figure 4. A comparison of the 2MASS default, Kron and extrapolated magnitudes in the J and K_S bands. The dots are a sample of the measured values of the galaxies in the matched 2MASS–2dFGRS catalogue. The solid and dotted lines indicate the median, 10 and 90 percentiles of the distribution.

photometry algorithms developed and employed 2MASS team and so in the final 2MASS data release the definitions of the Kron and extrapolated magnitudes may be slightly modified (Jarrett, private communication).

Fig. 4 compares the default, Kron and extrapolated magnitudes in the J and K_S bands for the matched 2MASS–2dFGRS catalogue. The upper panel shows that while the median offset between the J-band isophotal default magnitudes and the pseudo-total Kron magnitudes is small there is a large spread with some galaxies having default magnitudes more than 0.5 mag fainter than the Kron magnitude. The Kron magnitudes are systematically fainter than the extrapolated magnitudes by between approximately 0.1 and 0.3 mag. This offset is rather larger than expected: if the Kron radius is computed using a faint isophote to define the extent of the image from which the intensity weighted radius is measured, then the Kron magnitudes should be very close to total. For an
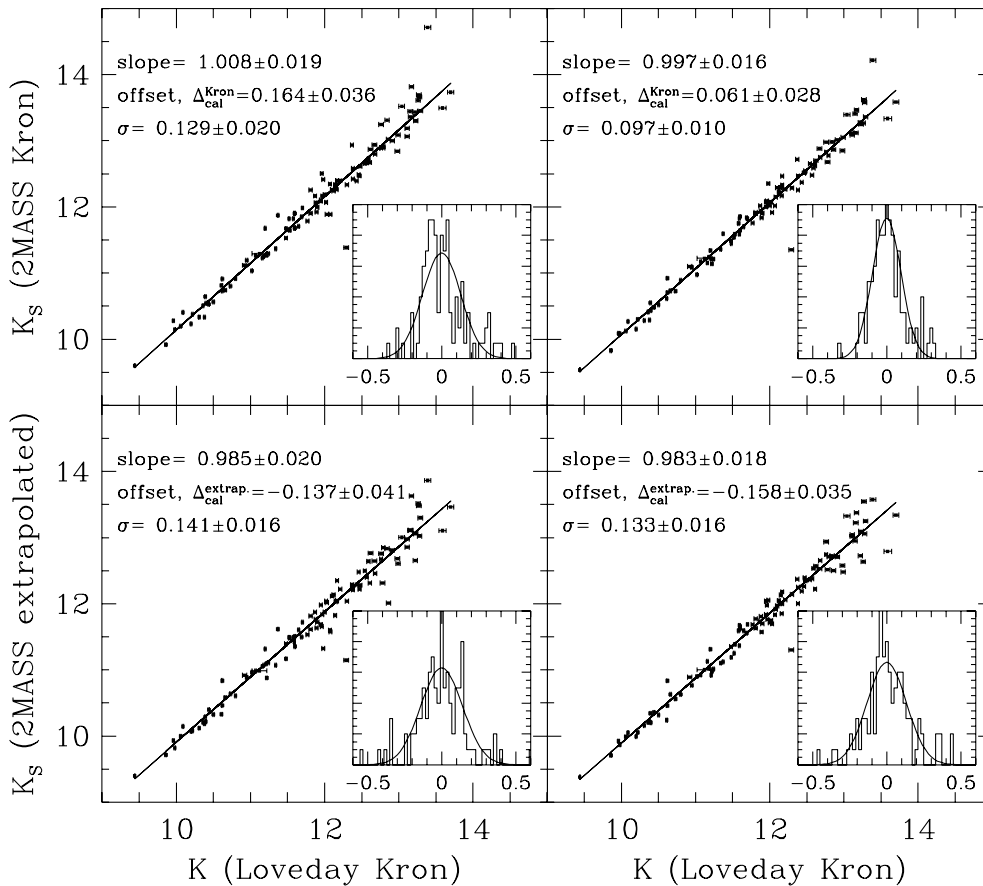
Figure 5. Comparison of 2MASS Kron and extrapolated magnitudes with the independent measurements of Loveday (2000). The left-hand panels are for the K_S-band Kron and extrapolated magnitudes (k_m_e and k_m_ext in the 2MASS data base). The right-hand panels show Kron and extrapolated magnitudes inferred from the 2MASS *J*-band Kron and extrapolated magnitudes, and the measured default aperture $J - K_S$ colours (j$_m$e–j$_m$ + k$_m$ and j$_m$ext–j$_m$ + k$_m$ in the 2MASS data base variables). The horizontal error bars show the measurement errors quoted by Loveday (2000). The solid lines show simple least-squares fits. The slopes and zero-point offsets of these fits and the rms residuals about the fits are indicated on each panel. The inset plots show the distribution of residual magnitude differences.

exponential light profile ($\beta = 1$), the Kron radius should capture 96 per cent of the flux, while for an $r^{1/4}$ law ($\beta = 4$), 90 per cent of the flux should be enclosed. In other words, the Kron magnitude should differ from the total magnitude by only 0.044 and 0.11 mag in these two cases. However, the choice of the isophote is a compromise between depth and statistical robustness. In the case of the 2MASS second incremental release, an isophote of 21.7(20.0) mag arcsec^{-2} in $J(K_S)$ was adopted (Jarrett, private communication). These relatively bright isophotes, particularly the K_S-band isophote, could lead to underestimates of the Kron radii and fluxes for lower surface brightness objects, and plausibly accounts for much of the median offset of 0.3 mag seen in Fig. 4 between the K_S-band Kron and extrapolated magnitudes. This line of reasoning favours adopting the extrapolated magnitudes as the best estimate of the total magnitudes, but, on the other hand, the extrapolated magnitudes are model-dependent and have larger measurement errors.

To understand better the offset and scatter in the 2MASS magnitudes we have compared a subset of the 2MASS data with the independent *K*-band photometry of Loveday (2000). The pointed observations of Loveday have better resolution than the 2MASS images and a good signal-to-noise ratio to a much deeper isophote. This enables accurate, unbiased Kron magnitudes to be measured. Note that the offset between the 2MASS K_S-band and the standard *K*-band used by Loveday is expected to be almost

completely negligible (see Carpenter 2001). The left-hand panels of Fig. 5 compare these measurements with the corresponding 2MASS Kron and extrapolated magnitudes. The right-hand panels show K_S -band Kron and extrapolated magnitudes computed by taking the 2MASS *J*-band Kron and extrapolated magnitudes and subtracting the $J - K_S$ colour measured within the default aperture. These indirect estimates are interesting to consider as they combine the profile information from the deeper *J*-band image with the $J - K_S$ colour measured within the largest aperture in which there is good signal-to-noise ratio. The straight lines plotted in Fig. 5 show simple least squares fits and the slope, and zero-point offset of these fits are indicated on each panel along with bootstrap error estimates. Also shown in the inset panels is the distribution of residual magnitude differences about each of the fits and a Gaussian fit to this distribution. The rms of these residuals and a bootstrap error estimate is also given in each panel.

From these comparisons we first see that all the fits have slopes entirely consistent with unity, but that their zero-points and scatters vary. The zero-point offsets, Δ_{cal}^{Kron}, between both the 2MASS Kron magnitude measurements and those of Loveday confirm that the 2MASS Kron magnitudes systematically underestimate the galaxy luminosities. In the case of the direct K_S-band 2MASS magnitudes the offset is $\Delta_{cal}^{Kron} = 0.164$ mag. In the case of the Kron magnitudes inferred from the deeper *J*-band image profiles, the offset is reduced to $\Delta_{cal}^{Kron} = 0.061$ mag. Conversely, the 2MASS extrapolated

magnitudes are systematically brighter than the Loveday Kron magnitudes by $-\Delta_{cal}^{extrap.} = 0.137$ and 0.158 mag, where one would expect an offset of only $\Delta_{Kron} = 0.044$ to 0.11 mag because of the difference in definition between ideal Kron and true total magnitudes. For both estimates of the extrapolated magnitude and for the directly estimated Kron magnitude the scatter about the correlation is approximately 0.14 mag and we note a slight tendency for the scatter to increase at faint magnitudes. The magnitude estimate that best correlates with the Loveday measurements is the Kron magnitude estimated from the 2MASS J-band Kron magnitude and the default aperture $J - K_S$ colour. Here the distribution of residuals has a much reduced scatter of only 0.1 mag and has very few outliers.

Our conclusions from the comparison of Kron magnitudes is that it is preferable to adopt the K_S-band magnitude inferred from the J-band Kron or extrapolated magnitude by converting to the K_S-band using default aperture colour, rather than to use the noisier and more biased direct K_S-band estimates. With this definition, we find that the 2MASS Kron magnitudes slightly underestimate the galaxy luminosities while the extrapolated magnitudes slightly overestimate the luminosities, particularly at faint fluxes. We will present results for both magnitude definitions, but we note that to convert to total magnitudes we
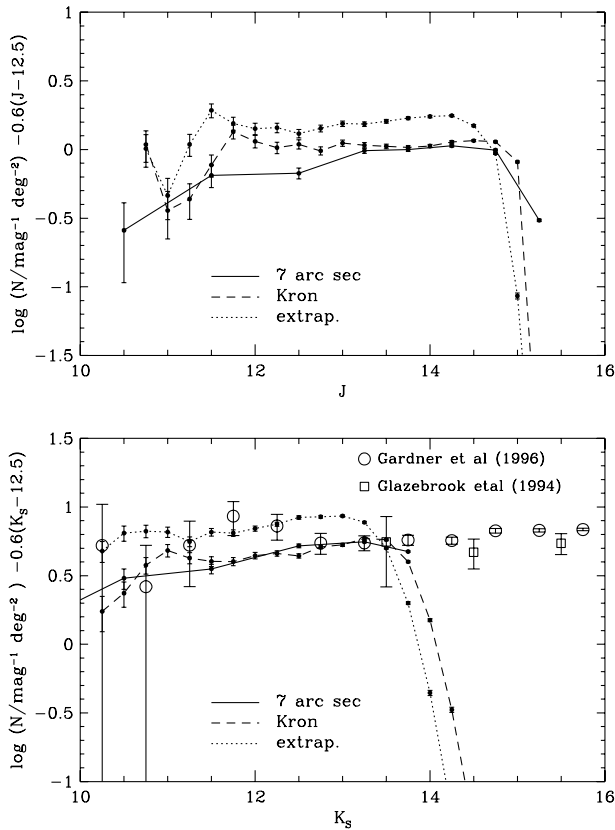
estimate that the 2MASS Kron magnitudes should be brightened by $\Delta_{cal}^{Kron} + \Delta_{Kron} = 0.1$–0.17 mag and the extrapolated magnitudes dimmed by $-\Delta_{cal}^{extrap.} - \Delta_{Kron} = 0.05$–0.11 mag.

2.4 Completeness of the 2MASS catalogue

Here we define the magnitude-limited samples which we will analyse in Section 4 and test them for possible incompleteness in both magnitude and surface brightness. For the Kron and extrapolated magnitudes, the 2MASS catalogue has high completeness to the nominal limits of $J < 14.7$ and $K_S < 13.9$. However, to ensure very high completeness and to avoid any bias in our luminosity function estimates, we made the following more conservative cuts. For the Kron magnitudes, we limited our sample to either $J < 14.45$ or $K_S < 13.2$, and for the extrapolated magnitudes to either $J < 14.15$ or $K_S < 12.9$. These choices are motivated by plots such as the top panel of Fig. 4. Here the isophotal default magnitude limit of $J < 14.7$ is responsible for the right-hand edge to the distribution of data points. One sees that this limit begins to remove objects from the distribution of Kron magnitudes for $J \gtrsim 14.5$. An indication that the survey is complete to our adopted limits is given by the number counts shown in Fig. 6, which only begin to roll over at fainter magnitudes.

More rigorously, we have verified that the samples are complete to these limits by examining their $V(z_i)/V(z_{max,i})$ distributions. Here, z_i is the redshift of a galaxy in the sample, $z_{max,i}$ is the maximum redshift at which this galaxy would satisfy the sample selection criteria, and $V(z)$ is the survey volume that lies at a redshift less than z. If the sample is complete and of uniform density, $V(z_i)/V(z_{max,i})$ is uniformly distributed within the interval 0–1. To evaluate z_{max} we made use of the default k+e corrections described in the following section, but the results are not sensitive
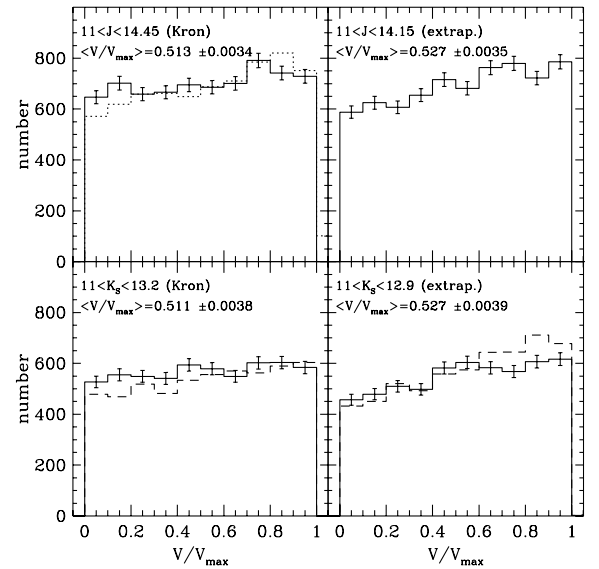

Figure 6. Differential galaxy number counts in the J and K_S bands, all with Poisson error bars and with a Euclidean slope subtracted so as to expand the scale of the ordinate. The J and K_S counts linked by the solid line are the 2MASS 7 arcsec aperture counts of Jarrett et al. (in preparation). The counts linked by the dashed and dotted lines are those of the 2MASS−2dFGRS redshift catalogue for Kron and extrapolated magnitudes, respectively. The K_S-band magnitudes are those inferred from the J-band magnitudes and aperture colours. In the K_S-band these are compared with the counts of Gardner et al. (1996) and Glazebrook et al. (1994) as indicated in the figure legend.

Figure 7. The distributions of V/V_{max} for our magnitude-limited samples. The solid histograms in the four panels show the V/V_{max} distributions for our J and K_S Kron and extrapolated magnitude-limited samples. The mean values of $\langle V/V_{max} \rangle$ are indicated on each panel. The K_S-band magnitudes are those inferred from the J-band magnitudes and aperture colours. The distributions for the directly measured K_S-band Kron and extrapolated magnitudes are shown by the dashed histograms in the lower panels. The dotted histogram in the top-left panel shows the V/V_{max} distribution we obtain, when attempting to take account of the 2MASS isophotal diameter and isophotal magnitude limits in estimating the V_{max} values.

to reasonable variations in the assumed corrections or in the cosmology. The solid histograms in Fig. 7 show these distributions for each of our four magnitude-limited samples. Note that the K_S-band magnitudes are those inferred from the J-band magnitudes and aperture colours. The dashed histograms in the lower panels show the corresponding distributions for the directly measured K_S-band magnitudes. In all these cases we have computed V_{max} simply from the imposed apparent magnitude limits and have ignored any possible dependence of the catalogue completeness on surface brightness.

If the samples were incomplete the symptom one would expect to see is a deficit in the V/V_{max} distributions at large V/V_{max} and hence a mean $\langle V/V_{max} \rangle < 0.5$. There is no evidence for such a deficit in these distributions. In fact each has a mean $\langle V/V_{max} \rangle$ slightly greater than 0.5. The slight gradient in the V/V_{max} distribution is directly related to the galaxy number counts shown in Fig. 6, which are slightly steeper than expected for a homogeneous, non-evolving galaxy distribution. A similar result has been found in the bright b_J-band counts (Maddox et al. 1990c). The b_J-band result has been variously interpreted as evidence for rapid evolution, systematic errors in the magnitude calibration, or a local hole or underdensity in the galaxy distribution (Maddox et al. 1990c; Shanks 1990; Metcalfe, Fong & Shanks 1995). Here we note that the gradient in the V/V_{max} distributions (and also in the galaxy counts) becomes steeper both as one switches from Kron to the less reliable extrapolated magnitudes and as one switches from the J-band data to the lower signal-to-noise K_S-band data. This gives strong support to our decision to adopt the K_S-band magnitudes derived from the J-band Kron and extrapolated magnitudes and aperture $J - K_S$ colours. It also cautions that the mean $\langle V/V_{max} \rangle > 0.5$ cannot necessarily be taken as a sign of evolution or a local underdensity, but may instead be related to the accuracy of the magnitude measurements. The comparison to the observations of Loveday (2000) shows no evidence for systematic errors in the magnitudes, but does not constrain the possibility that the distribution of magnitude measurement errors may become broader or skewed at fainter magnitudes. Such variations would affect the V/V_{max} distributions and could produce the observed behaviour. We conclude by noting that while the shift in the mean $\langle V/V_{max} \rangle$ is statistically significant, it is nevertheless small for the samples we analyse and has little effect on the resulting luminosity function estimates.

We now investigate explicitly the degree to which the completeness of the 2MASS catalogue depends on surface brightness by estimating V_{max} as a function of both absolute magnitude and surface brightness. This is an important issue: if the catalogue is missing low surface brightness galaxies our estimates of the luminosity function will be biased. The approach we have taken follows that developed in Cross et al. (2001) for the 2dFGRS. We estimate an effective central surface brightness, μ_0^z, for each observed galaxy assuming an exponential light distribution, that the Kron magnitudes are total and that the Kron radii are exactly five exponential scalelengths. This is then corrected to redshift $z = 0$ using

$$\mu_0 = \mu_0^z - 10\log(1 + z) - k(z) - e(z) \tag{2.1}$$

to account for redshift dimming and k+e corrections (cf. Section 3). Note that in the 2MASS catalogue, galaxies with estimated Kron radii less than 7 arcsec, have their Kron radii set to 7 arcsec. This will lead us to underestimate the central surface brightnesses of these galaxies, but this will only affect high surface
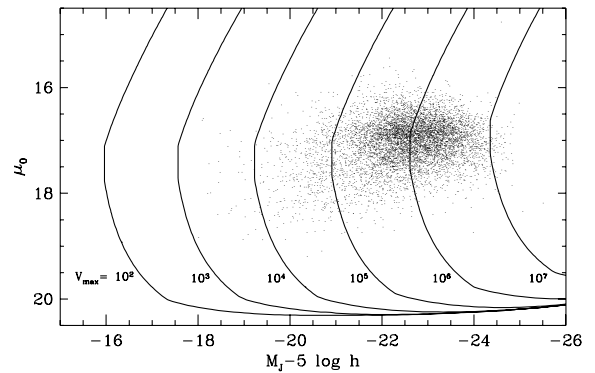

Figure 8. The points show the distribution of the estimated central surface brightness, μ_0, and absolute magnitude, M_J, for our $J < 14.45$ (Kron) sample. The contours show visibility theory estimates of V_{max} as a function of μ_0 and M_J. The contours are labelled by their V_{max} values in units of $(\text{Mpc } h^{-1})^3$.

brightness objects and will not affect whether a galaxy can or cannot be seen. The distribution in the M_J–μ_0 plane of our Kron J-band selected sample is shown by the points in Fig. 8.

Cross et al. (2001) use two different methods to estimate the value of V_{max} associated with each position in this plane. The first method uses the visibility theory of Phillipps, Davies & Disney (1990). We model the selection characteristics of the 2MASS Extended Source Catalogue by a set of thresholds. The values appropriate in the J-band are a minimum isophotal diameter of 8.5 arcsec at an isophote of 20.5 mag arcsec^{-2}, and an isophotal magnitude limit of $J < 14.7$ at an isophote of 21.0 mag arcsec^{-2} (Jarrett et al. 2000). In addition, we impose the limits in the Kron magnitude of $11 < J < 14.45$ that define the sample we analyse. We then calculate for each point on the M_J–μ_0 plane the redshift at which such a galaxy will drop below one or other of these selection thresholds and hence compute a value of V_{max}. The results of this procedure are shown by the contours of constant V_{max} plotted in Fig. 8. Note that these estimates of V_{max} are only approximate since we have made the crude assumption that all the galaxies are circular exponential discs. In addition, the diameter and isophotal limits are only approximate and vary with observing conditions.

The second method developed by Cross et al. (2001) consists of making an empirical estimate of V_{max} in bins in the M_J–μ_0 plane. They look at the distribution of observed redshifts in a given bin and adopt the 90th percentile of this distribution to define z_{max} and hence V_{max}. It is more robust to use the 90th percentile rather than the 100th percentile and the effect of this choice can easily be compensated for when estimating the luminosity function (Cross et al. 2001). Note that in our application to the 2MASS data we do not apply corrections for incompleteness or for the effects of clustering. The result of this procedure is to confirm that for the populated bins, the V_{max} values given by the visibility theory are a good description of the data.

In Fig. 8 we see that the distribution of galaxies in the M_J–μ_0 plane is well separated from the low surface brightness limit of approximately 20.5 mag arcsec^{-2}, where the V_{max} contours indicate that the survey has very little sensitivity. Thus, there is no evidence that low surface brightness galaxies are missing from the 2MASS catalogue. Furthermore, in the region occupied by the observed data, the V_{max} contours are close to the vertical indicating that there is little dependence of V_{max} on surface brightness. The way in which the V/V_{max} distribution is modified by including this estimate of the surface brightness dependence is shown by the
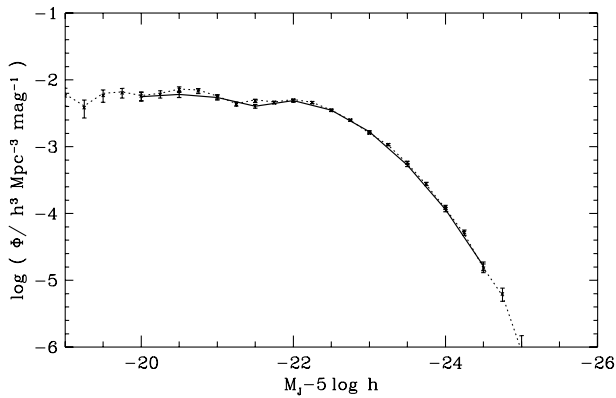
Figure 9. Three $1/V_{max}$ estimates of the Kron J-band luminosity function. The data points with error bars show the estimate based on the assumption that V_{max} depends only upon absolute magnitude and ignoring any possible surface brightness dependence. The dotted line and heavy solid line show the estimates in which the surface brightness dependence of V_{max} is derived from the visibility theory and from the empirical method of Cross et al. (2001), respectively.
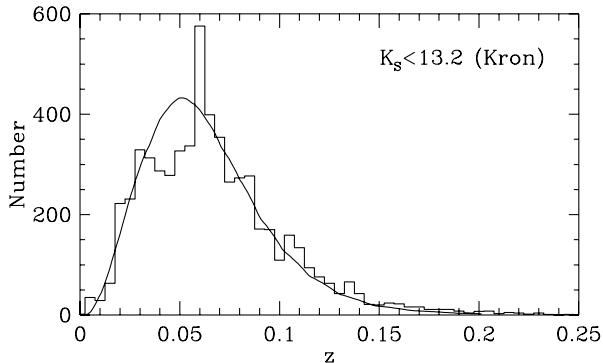

Figure 10. The redshift distribution of the $K_S < 13.2$ (Kron) sample selected from the matched 2MASS–2dFGRS catalogue. The smooth curve is the model prediction based on the SWML estimate of the K_S-band luminosity function (cf. Section 4). The model prediction is very insensitive to the assumed k+e correction and cosmology.

dotted histogram in the top-left panel of Fig. 7. Its effect is to increase the mean V/V_{max} slightly, suggesting that this estimate perhaps overcorrects for the effect of surface brightness selection. Even so, the change in the estimated luminosity function is negligible as confirmed by the three estimates of the Kron J-band luminosity function shown in Fig. 9. These are all simple $1/V_{max}$ estimates, but with V_{max} computed either ignoring surface brightness effects or using one of the two methods described above. These luminosity functions differ negligibly, indicating that no bias is introduced by ignoring surface brightness selection effects.

3 MODELLING THE STELLAR POPULATIONS

The primary aim of this paper is to determine the present-day J and K_S-band luminosity functions and also the stellar mass function of galaxies. Since the 2MASS survey spans a range of redshift (see Fig. 10), we must correct for both the redshifting of the filter bandpass (k-correction) and for the effects of galaxy evolution (e-correction). In practice, the k and e-corrections at these wavelengths are both small and uncertainties in them have little

effect on the estimated luminosity functions. This is because these infrared bands are not dominated by young stars and also because the 2MASS survey does not probe a large range of redshift. We have chosen to derive individual k and e-corrections for each galaxy using the stellar population synthesis models of Bruzual & Charlot (1993; in preparation). We have taken this approach not because such detailed modelling is necessary to derive robust luminosity functions, but because it enables us to explore the uncertainties in the derived galaxy stellar mass functions, which are, in fact, dominated by uncertainties in the properties of the stellar populations.

The latest models of Bruzual & Charlot (in preparation) provide, for a variety of different stellar initial mass functions (IMFs), the spectral energy distribution (SED), $l_\lambda(t, Z)$, of a single population of stars formed at the same time with a single metallicity, as a function of both age, t, and metallicity, Z. We convolve these with an assumed star formation history, $\psi(t')$, to compute the time-evolving SED of the model galaxy,

$$L_\lambda(t) = \int_0^t l_\lambda(t - t', Z)\psi(t')\,dt'. \tag{3.1}$$

We take account of the effect of dust extinction on the SEDs using the Ferrara et al. (1999) extinction model normalized so that the V-band central face-on optical depth of the Milk-Way is 10. This value corresponds to the mean optical depth of L_* galaxies in the model of Cole et al. (2000) which employs the same model of dust extinction. We assume a typical inclination angle of 60° which yields a net attenuation factor of 0.53 in the V-band and 0.78 in the J-band. By varying the assumed metallicity, Z, and star formation history, we build up a two-dimensional grid of models. Then, for each of these models, we extract tracks of $b_J - K_S$ and $J - K_S$ colours and the stellar mass-to-light ratio as a function of redshift.

Our standard set of tracks assumes a cosmological model with $\Omega_0 = 0.3$, $\Lambda_0 = 0.7$, Hubble constant $H_0 = 70\,\mathrm{km\,s^{-1}\,Mpc^{-1}}$, and star formation histories with an exponential form, $\psi(t) \propto \exp{-[t(z) - t(z_f)]/\tau}$. Here, $t(z)$ is the age of the Universe at redshift z and the galaxy is assumed to start forming stars at $z_f = 20$. For these tracks, we adopt the Kennicutt IMF (Kennicutt 1983) and include the dust extinction model. The individual tracks are labelled by a metallicity, Z, which varies from $Z = 0.0001$ to 0.05 and a star formation time-scale, τ, which varies from $\tau = 1$ to 50 Gyr. Examples of these tracks are shown in Fig. 11, along with the observed redshifts and colours of the 2MASS galaxies. We can see that the infrared $J - K_S$ colour depends mainly on metallicity while the $b_J - K_S$ colour depends both on metallicity and on the star formation time-scale. Thus, the use of both colours allows a unique track to be selected. Note from the bottom panel that, for all the tracks, the k+e correction is always small for the range of redshift spanned by our data.

We can gauge how robust our results are by varying the assumptions of our model. In particular, we vary the IMF, the dust extinction and cosmological models, and include or exclude the evolutionary contribution to the k+e correction. Also, we consider power-law star formation histories, $\psi(t) \propto [t(z)/t(z_f)]^{-\gamma}$, as an alternative to the exponential model. The results are discussed in the beginning of Section 5.

The procedure for computing the individual galaxy k+e corrections is straightforward. At the measured redshift of a galaxy, we find the model whose $b_J - K_S$ and $J - K_S$ colours most closely match that of the observed galaxy. Having selected the model we then follow it to $z = 0$ to predict the present-day J and K_S-band
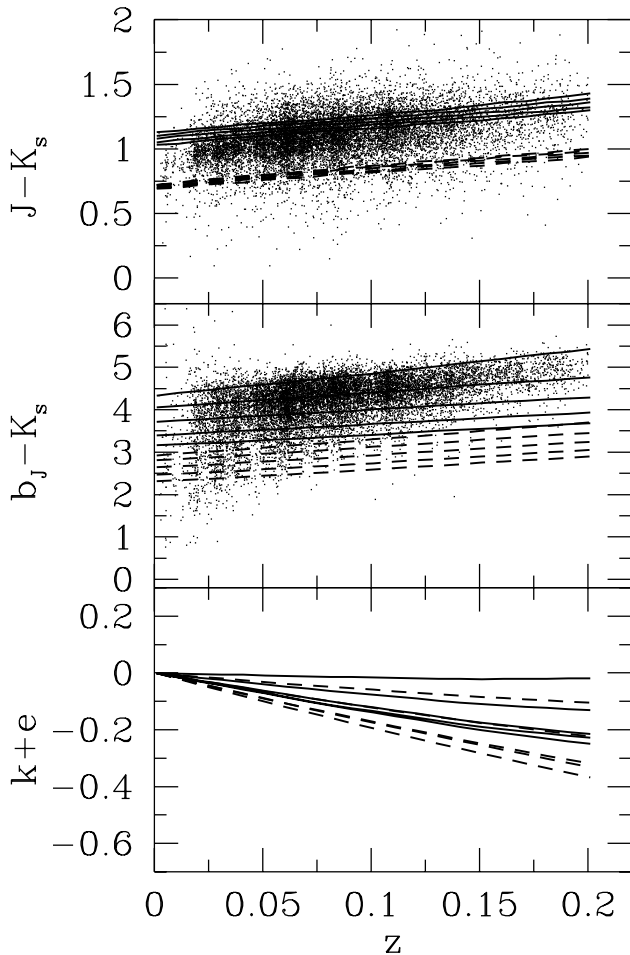
Figure 11. The points in the upper two panels show the observed distributions of $J-K_S$ and $b_J - K_S$ colours as a function of redshift for our matched 2MASS–2dFGRS catalogue with $z < 0.2$ and $J < 14.45$ (Kron). Overlaid on these points are some examples of model tracks. The solid curves are for solar metallicity, $Z = 0.02$, and the dashed curves for $Z = 0.004$. Within each set, the tracks show different choices of the star formation time-scale, τ. The grid of values we use has $\tau = 1, 3, 5, 10$ and 50 Gyr. Shorter values of τ lead to older stellar populations and redder colours. The bottom panel shows the k+e corrections in the J-band for these same sets of tracks.

luminosities of the galaxy and also its total stellar mass. We also use the model track to follow its k+e correction to higher redshift in order to compute z_{max}, the maximum redshift at which this galaxy would have passed the selection criteria for inclusion into the analysis sample.

4 LUMINOSITY FUNCTION ESTIMATION

We use both the simple $1/V_{max}$ method and standard maximum likelihood methods to estimate the luminosity functions. We present Schechter function fits computed using the STY method (Sandage, Tammann & Yahil 1978) and also non-parametric estimates using the stepwise maximum likelihood method (SWML) of Efstathiou, Ellis & Peterson (1988). Our implementation of each of these methods is described and tested in Norberg et al. (in preparation). The advantage of the maximum likelihood methods is that they are not affected by galaxy clustering (provided that the galaxy luminosity function is independent of galaxy

density). By contrast the $1/V_{max}$ method, which makes no assumption about the dependence of the luminosity function with density, is subject to biases produced by density fluctuations.

The two maximum likelihood methods determine the shape of the luminosity function, but not its overall normalization. We have chosen to normalize the luminosity functions by matching the galaxy number counts of Jarrett et al. (in preparation). These were obtained from a 184 deg^2 area selected to have low stellar density and in which all the galaxy classifications have been confirmed by eye. The counts are reproduced in Fig. 6. By using the same 7 arcsec aperture magnitudes as used by Jarrett et al. (in preparation) and scaling the galaxy counts in our redshift survey, we deduce that the effective area of our redshift catalogue is 619 ± 25 deg^2. Note that normalizing in this way by-passes the problem of whether or not some fraction of the missed 2MASS objects are stars. Fig. 6 also shows the Kron and extrapolated magnitude J and K_S counts of the 2MASS–2dFGRS redshift survey. In the lower panel, these counts are seen to be in agreement with the published K-band counts of Glazebrook et al. (1994) and Gardner et al. (1996).

We also checked the normalization using the following independent estimate of the effective solid angle of the redshift survey. For galaxies in the 2dFGRS parent catalogue brighter than $b_J < B_{limit}$, we computed the fraction that have both measured redshifts and match a 2MASS galaxy. For a faint B_{limit} this fraction is small as the 2dFGRS catalogue is much deeper than the 2MASS catalogue, but as B_{limit} is made brighter, the fraction asymptotes to the fraction of the area of the 2dFGRS parent catalogue covered by the joint 2MASS–2dFGRS redshift survey. By this method we estimate that the effective area of our redshift catalogue is 642 ± 22 deg^2, which is in good agreement with the estimate from the counts of Jarrett et al. (in preparation).

It should be noted that for neither of these estimates of the effective survey area do the quoted uncertainties take account of variations in the number counts because of the large-scale structure. To estimate the expected variation in the galaxy number counts within the combined 2MASS–2dFGRS survey arising from the large-scale structure we constructed an ensemble of mock catalogues from the ΛCDM Hubble volume simulation of the VIRGO consortium [Evrard 1999; Evrard et al. (in preparation); http://www.physics.lsa.umich.edu/hubble-volume]. Mock 2dFGRS catalogues constructed from the VIRGO Hubble Volume simulations (Baugh et al., in preparation) can be found at http://star-www.dur.ac.uk/n~cole/mocks/hubble.html. We simply took these catalogues and sampled them to the depth of 2MASS over a solid angle of 619 deg^2. To this magnitude limit we found an rms variation of 15 per cent in the number of galaxies. We took this to be a realistic estimate of the uncertainty in the 2MASS number counts and propagated this error through when computing the error on the normalization of the luminosity function.

5 RESULTS

5.1 Luminosity functions

Fig. 12 shows SWML estimates of the Kron J and K_S luminosity functions. The points with error bars show results for our default choice of k+e corrections, namely those obtained for an $\Omega_0 = 0.3$, $\Lambda_0 = 0.7$, $H_0 = 70$ km s^{-1} Mpc^{-1} cosmology with a Kennicutt IMF and including dust extinction. The figure also illustrates that the luminosity functions are very robust to varying this set of assumptions. The various curves in each plot are estimates made
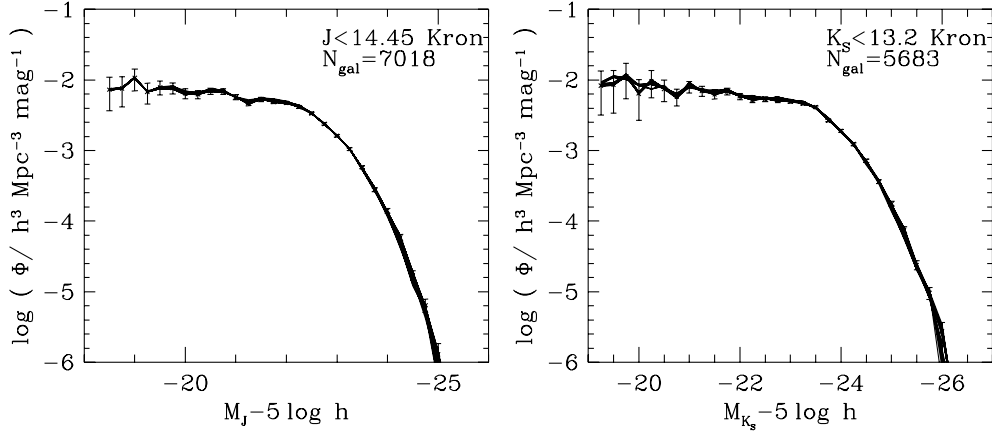
Figure 12. SWML estimates of the Kron magnitude J (left) and K_S-band (right) luminosity functions (points with error bars). Our default model of k+e corrections (Kennicutt IMF and standard dust extinction) is adopted. The set of curves on each plot shows the effects of neglecting dust extinction, and/or switching to a Salpeter IMF, and/or changing the Hubble constant to $H_0 = 50\,\mathrm{km\,s^{-1}\,Mpc^{-1}}$, and/or adopting power-law star formation histories, and/or making a k-correction but no evolution correction.

Table 1. The dependence of the J and K_S-band Schechter function parameters on cosmological parameters and evolutionary corrections. The parameters refer to STY estimates of the luminosity function for the 2MASS Kron magnitudes and are derived using the k or k+e corrections based on model tracks that include dust extinction and assume the Kennicutt IMF. To convert to total magnitudes we estimate that the M^* values should be brightened by between $\Delta_{\mathrm{Kron}} + \Delta_{\mathrm{cal}}^{\mathrm{Kron}} - \Delta_{\mathrm{conv}} = 0.08$ and 0.15 mag. Note that the statistical errors we quote for the Φ_* values include the significant contribution that we estimate is induced by large-scale structure.

| Ω_0	Λ_0	Model tracks	$M_J^* - 5\log h$	α_J	Φ_J^* (h^3 Mpc^{-3})	$M_{K_S}^* - 5\log h$	α_{K_S}	$\Phi_{K_S}^*$ (h^3 Mpc^{-3})
0.3	0.7	k+e	-22.36 ± 0.02	-0.93 ± 0.04	$1.04 \pm 0.16 \times 10^{-2}$	-23.44 ± 0.03	-0.96 ± 0.05	$1.08 \pm 0.16 \times 10^{-2}$
0.3	0.7	k only	-22.47 ± 0.02	-0.99 ± 0.04	$0.90 \pm 0.14 \times 10^{-2}$	-23.51 ± 0.03	-1.00 ± 0.04	$0.98 \pm 0.15 \times 10^{-2}$
0.3	0.0	k+e	-22.29 ± 0.03	-0.89 ± 0.04	$1.16 \pm 0.18 \times 10^{-2}$	-23.36 ± 0.03	-0.93 ± 0.05	$1.21 \pm 0.18 \times 10^{-2}$
0.3	0.0	k only	-22.38 ± 0.03	-0.95 ± 0.04	$1.02 \pm 0.15 \times 10^{-2}$	-23.43 ± 0.03	-0.96 ± 0.05	$1.10 \pm 0.16 \times 10^{-2}$
1.0	0.0	k+e	-22.22 ± 0.02	-0.87 ± 0.03	$1.26 \pm 0.19 \times 10^{-2}$	-23.28 ± 0.03	-0.89 ± 0.05	$1.34 \pm 0.20 \times 10^{-2}$
1.0	0.0	k only	-22.34 ± 0.02	-0.93 ± 0.04	$1.08 \pm 0.16 \times 10^{-2}$	-23.38 ± 0.03	-0.93 ± 0.05	$1.18 \pm 0.17 \times 10^{-2}$
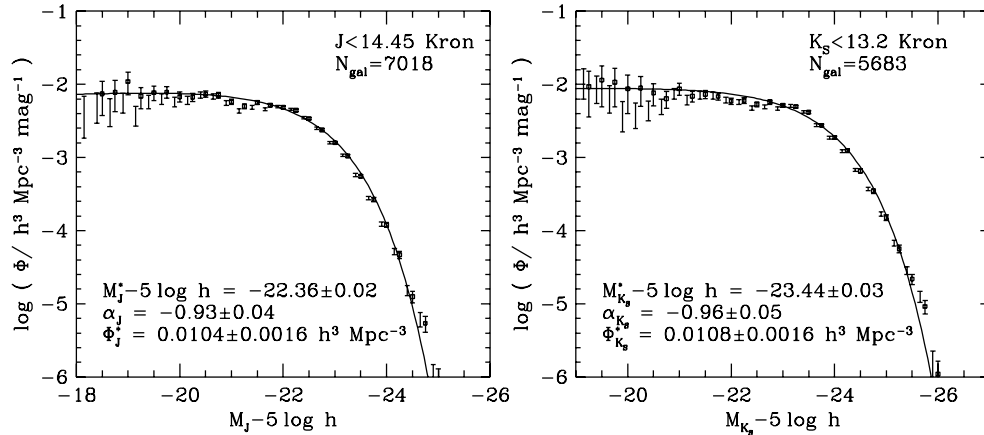
Figure 13. SWML estimates of the Kron magnitude J (left) and K_S-band (right) luminosity functions (data points with error bars), and STY Schechter function estimates (lines). The parameter values and error estimates of the Schechter functions are given in the legends. The error bars without data points show $1/V_{\mathrm{max}}$ estimates of the luminosity functions. For clarity these have been displaced to the left by 0.1 mag.

neglecting dust extinction, and/or switching to a Salpeter IMF, and/or changing the Hubble constant to $H_0 = 50\,\mathrm{km\,s^{-1}\,Mpc^{-1}}$, and/or adopting power-law star formation histories, and/or making a k-correction but no evolution correction. The systematic shifts caused by varying these assumptions are all comparable with or smaller than the statistical errors. The biggest shift results from applying or neglecting the evolutionary correction. In terms of the characteristic luminosity in the STY Schechter function fit, the

estimates which include evolutionary corrections are 0.05–0.1 mag fainter than those that only include k-corrections (see Table 1).

In Fig. 13 we compare $1/V_{\mathrm{max}}$ and SWML Kron luminosity function estimates (for our default choice of k+e corrections) with STY Schechter function estimates. In general, the luminosity functions are well fit by Schechter functions, but there is a marginal evidence for an excess of very luminous galaxies over that expected from the fitted Schechter functions. We tabulate the

SWML estimates in Table 2. Integrating over the luminosity function gives luminosity densities in the J and K_S-bands of $\rho_J = (2.75 \pm 0.41) \times 10^8 \, h \, L_\odot \, \mathrm{Mpc}^{-3}$ and $\rho_{K_S} = (5.74 \pm 0.86) \times 10^8 \, h \, L_\odot \, \mathrm{Mpc}^{-3}$ respectively, where we have adopted $M_J^\odot = 3.73$ and $M_{K_S}^\odot = 3.39$ (Johnson 1966; Allen 1973). In this analysis, we have not taken account of the systematic and random measurement errors in the galaxy magnitudes. In the case of the STY estimate, the random measurement errors can be accounted for by fitting a Schechter function which has been convolved with the distribution of magnitude errors. However, for the Kron magnitudes, the rms measurement error is only 0.1 mag, as indicated by the comparison in the top right-hand panel of Fig. 5, and such a convolution has only a small effect on the resulting Schechter function parameters. We find that the only parameter that is affected is M^* which becomes fainter by just $\Delta_{\mathrm{conv}} = 0.02$ mag. The comparison to the Loveday (2000) data also indicates a systematic error in the 2MASS Kron magnitudes of $\Delta_{\mathrm{cal}}^{\mathrm{Kron}} = 0.061 \pm 0.031$. Combining these two systematic errors results in a net brightening of M^* by $\Delta_{\mathrm{cal}}^{\mathrm{Kron}} - \Delta_{\mathrm{conv}} = 0.041 \pm 0.031$ mag. As this net systematic error is both small and uncertain we have chosen not 0to apply a correction to our quoted Kron magnitude luminosity function parameters. We also recall that to convert from Kron to total magnitudes requires brightening M^* by between $\Delta_{\mathrm{Kron}} = 0.044$ and 0.11 depending on whether the luminosity profile of a typical galaxy is fit well by an exponential or $r^{1/4}$ law.

Fig. 14 shows the SWML and STY luminosity function estimates for samples defined by the 2MASS extrapolated, rather than Kron, magnitudes. With this definition of magnitude, the luminosity functions differ significantly from those estimated using the Kron magnitudes. In particular, the characteristic luminosities are 0.34 and 0.28 mag brighter in J and K_S, respectively. Most of this difference is directly related to the systematic offset in the J-band Kron and extrapolated magnitudes, which can be seen in either the middle panel of Fig. 4 or in the right-hand panels of Fig. 5 to be approximately 0.23 mag. Note that even in the K_S-band, it is this J-band offset that is relevant, as the K_S-band magnitudes we use are derived from the J-band values using the measured aperture colours. We have argued in Section 2.3 that this offset is caused by the J-band Kron 2MASS magnitudes being fainter than the true total magnitudes by between $\Delta_{\mathrm{cal}}^{\mathrm{Kron}} + \Delta_{\mathrm{Kron}} = 0.1$ and 0.17 and the extrapolated magnitudes being systematically too bright by $-\Delta_{\mathrm{cal}}^{\mathrm{extrap.}} - \Delta_{\mathrm{Kron}} = 0.05$–0.11 mag. Subtracting this 0.23 mag

Table 2. The SWML J and K_S-band luminosity functions for Kron magnitudes as plotted in Fig. 13. The units of both ϕ and its uncertainty $\Delta\phi$ are number per $h^{-3} \, \mathrm{Mpc}^3$ per magnitude.

$M - 5\log h$	$\phi_J \pm \Delta\phi_J$	$\phi_{K_S} \pm \Delta\phi_{K_S}$
-18.00	$(5.73 \pm 3.58) \times 10^{-3}$	$(3.13 \pm 3.64) \times 10^{-3}$
-18.25	$(5.38 \pm 3.34) \times 10^{-3}$	$(8.26 \pm 6.68) \times 10^{-3}$
-18.50	$(7.60 \pm 3.75) \times 10^{-3}$	
-18.75	$(7.94 \pm 3.59) \times 10^{-3}$	$(4.65 \pm 4.10) \times 10^{-3}$
-19.00	$(1.11 \pm 3.82) \times 10^{-2}$	$(5.76 \pm 4.32) \times 10^{-3}$
-19.25	$(6.98 \pm 2.26) \times 10^{-3}$	$(9.16 \pm 5.67) \times 10^{-3}$
-19.50	$(8.14 \pm 1.80) \times 10^{-3}$	$(1.12 \pm 0.64) \times 10^{-2}$
-19.75	$(8.17 \pm 1.45) \times 10^{-3}$	$(1.05 \pm 0.57) \times 10^{-2}$
-20.00	$(7.16 \pm 1.12) \times 10^{-3}$	$(8.58 \pm 4.63) \times 10^{-3}$
-20.25	$(6.62 \pm 0.88) \times 10^{-3}$	$(8.82 \pm 3.86) \times 10^{-3}$
-20.50	$(7.30 \pm 0.76) \times 10^{-3}$	$(6.94 \pm 2.44) \times 10^{-3}$
-20.75	$(7.07 \pm 0.64) \times 10^{-3}$	$(6.09 \pm 1.63) \times 10^{-3}$
-21.00	$(5.84 \pm 0.48) \times 10^{-3}$	$(9.26 \pm 1.69) \times 10^{-3}$
-21.25	$(4.97 \pm 0.39) \times 10^{-3}$	$(6.96 \pm 1.18) \times 10^{-3}$
-21.50	$(5.69 \pm 0.35) \times 10^{-3}$	$(7.29 \pm 0.98) \times 10^{-3}$
-21.75	$(5.15 \pm 0.28) \times 10^{-3}$	$(6.99 \pm 0.79) \times 10^{-3}$
-22.00	$(4.89 \pm 0.21) \times 10^{-3}$	$(5.98 \pm 0.61) \times 10^{-3}$
-22.25	$(4.49 \pm 0.17) \times 10^{-3}$	$(5.93 \pm 0.52) \times 10^{-3}$
-22.50	$(3.41 \pm 0.12) \times 10^{-3}$	$(5.39 \pm 0.42) \times 10^{-3}$
-22.75	$(2.37 \pm 0.09) \times 10^{-3}$	$(5.85 \pm 0.37) \times 10^{-3}$
-23.00	$(1.59 \pm 0.06) \times 10^{-3}$	$(5.24 \pm 0.28) \times 10^{-3}$
-23.25	$(1.06 \pm 0.04) \times 10^{-3}$	$(4.96 \pm 0.22) \times 10^{-3}$
-23.50	$(5.41 \pm 0.27) \times 10^{-4}$	$(4.18 \pm 0.17) \times 10^{-3}$
-23.75	$(2.66 \pm 0.17) \times 10^{-4}$	$(2.72 \pm 0.11) \times 10^{-3}$
-24.00	$(1.19 \pm 0.10) \times 10^{-4}$	$(1.88 \pm 0.08) \times 10^{-3}$
-24.25	$(4.69 \pm 0.54) \times 10^{-5}$	$(1.21 \pm 0.06) \times 10^{-3}$
-24.50	$(1.20 \pm 0.22) \times 10^{-5}$	$(6.54 \pm 0.37) \times 10^{-4}$
-24.75	$(5.40 \pm 1.34) \times 10^{-6}$	$(3.46 \pm 0.23) \times 10^{-4}$
-25.00	$(5.42 \pm 3.88) \times 10^{-7}$	$(1.48 \pm 0.13) \times 10^{-4}$
-25.25		$(5.55 \pm 0.65) \times 10^{-5}$
-25.50		$(2.13 \pm 0.33) \times 10^{-5}$
-25.75		$(9.42 \pm 1.96) \times 10^{-6}$
-26.00		$(1.09 \pm 0.56) \times 10^{-6}$

offset results in Kron and extrapolated luminosity functions that differ in M^* by only 0.11 mag. In the K_S-band, the faint end slope of the best-fitting Schechter function is significantly steeper in the extrapolated magnitude case, but note that this function is not a good description of the faint end of the luminosity function since the SWML and $1/V_{\mathrm{max}}$ estimates lie systematically below it. The
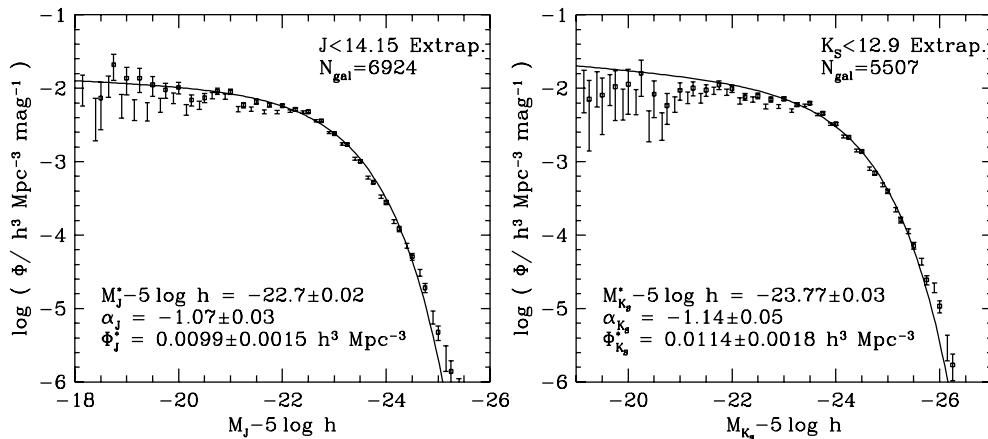

Figure 14. SWML estimates of the extrapolated magnitude J (left) and K_S-band (right) luminosity functions (data points with error bars), and STY Schechter function estimates (lines). The parameter values and error estimates of the Schechter functions are given in the legends. The error bars without data points show $1/V_{\mathrm{max}}$ estimates of the luminosity functions. For clarity these have been displaced to the left by 0.1 mag.

Schechter function fit is constrained mainly around M_*, and in this case the χ^2 value indicates it is not a good fit overall.

The residual differences between the Kron and extrapolated magnitude luminosity functions arise from the scatter in the relation between extrapolated and Kron magnitudes. If this scatter is dominated by the measurement error, then these differences represent small biases, which are largest for the less robust, extrapolated magnitudes. However, it is possible that the scatter is a result of genuine variations in the galaxy morphology and light profiles. To assess which of these alternatives is correct requires independent deep photometry of a sample of 2MASS galaxies to quantify the accuracy of the extrapolated magnitudes. However, we note that the V/V_{max} distributions for the extrapolated magnitudes shown in Fig. 7 have mean $\langle V/V_{max}\rangle$ values significantly greater than 0.5, which is probably an indication that the extrapolated magnitudes are not robust. Thus, overall we favour adopting Kron
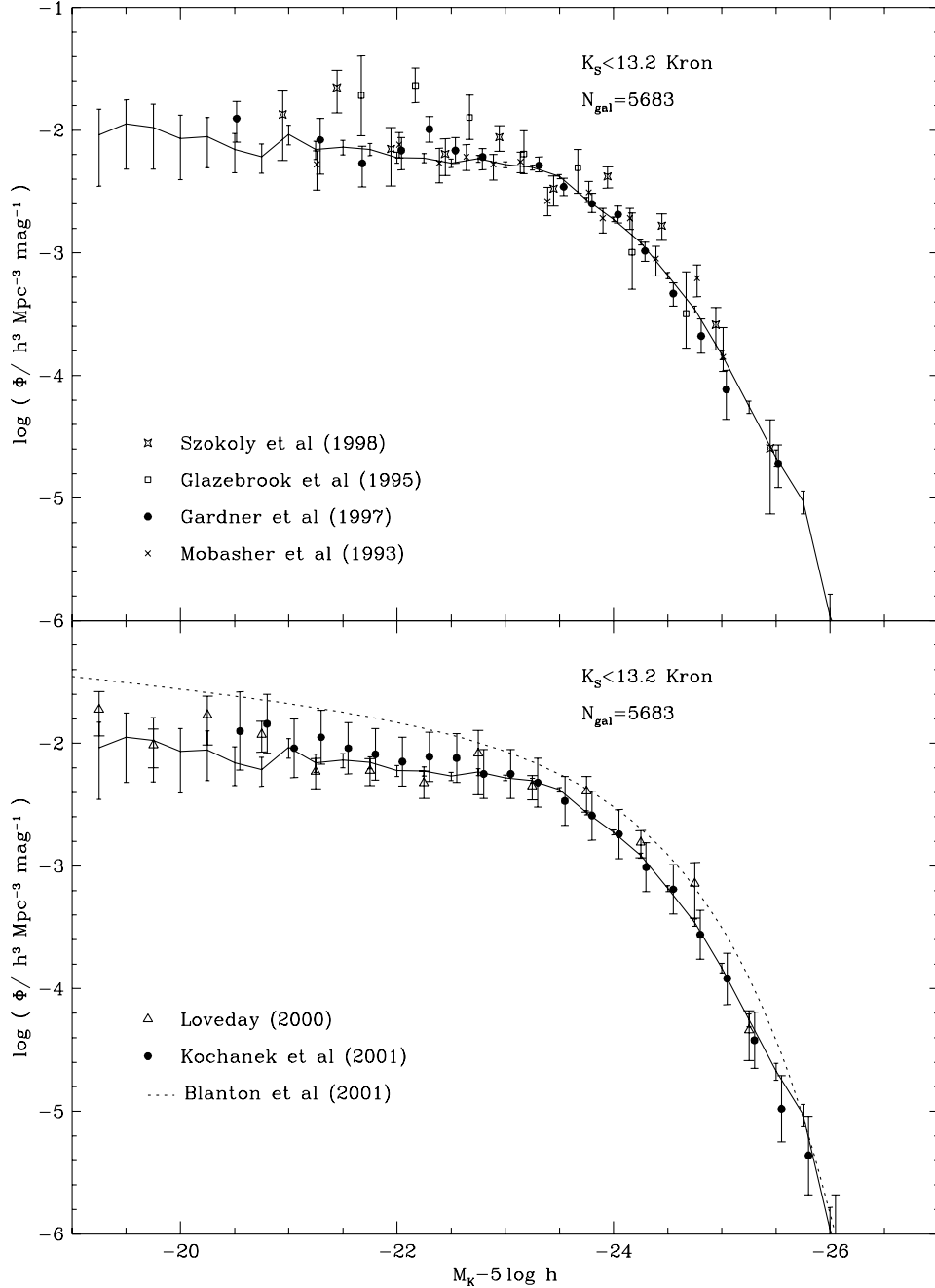

Figure 15. Comparison of various estimates of the K-band luminosity function. In both panels the solid line shows our SWML estimate of the K_S-band luminosity function for Kron magnitudes. The symbols and error bars in the top panel show the estimates of Mobasher et al. (1993), Glazebrook et al. (1995), Gardner et al. (1997) and Szokoly et al. (1998) as indicated in the legend. We have shifted the data of Glazebrook et al. (1995) brightward by 0.3 mag and the data of Mobasher et al. (1993) faintward by 0.22 mag as advocated by Glazebrook et al. (1995) to make aperture corrections and consistent k-corrections, respectively. In the lower panel the symbols and error bars show the recent estimates of Loveday (2000) and Kochanek et al. (2001). The estimate of Kochanek et al. has been shifted brightward by 0.05 mag to account for the difference between isophotal and Kron magnitudes. The dotted line shows a Schechter function estimate of the K-band luminosity function inferred from SDSS z^*-band luminosity function of Blanton et al. (2001) (see text for details).

Table 3. Schechter function fits to *K*-band luminosity functions. Where necessary, the values quoted have been converted from the cosmological model assumed in the original work to the $\Omega_0 = 0.3$, $\Lambda_0 = 0.7$ cosmology assumed here. In addition, we have shifted the M_K^* of Kochanek et al. (2001) brightward by 0.05 mag corresponding to the mean difference between 2MASS Kron and isophotal magnitudes in the Kochanek et al. sample. We have also shifted M_K^* of Glazebrook et al. (1995) brightward by 0.3 mag and that of Mobasher et al. (1993) faintward by 0.22 mag as advocated by Glazebrook et al. (1995) to make aperture corrections and consistent *k*-corrections, respectively.

Sample	M_K^*	α_K	$\Phi_K (h^3 \, \text{Mpc}^{-3})$
Mobasher et al. (1993)	-23.37 ± 0.30	1.0 ± 0.3	$1.12 \pm 0.16 \times 10^{-2}$
Glazebrook et al. (1995)	-23.14 ± 0.23	1.04 ± 0.3	$2.22 \pm 0.53 \times 10^{-2}$
Gardner et al. (1997)	-23.30 ± 0.17	1.0 ± 0.24	$1.44 \pm 0.20 \times 10^{-2}$
Szokoly et al. (1998)	-23.80 ± 0.30	1.3 ± 0.2	$0.86 \pm 0.29 \times 10^{-2}$
Loveday (2000)	-23.58 ± 0.42	1.16 ± 0.19	$1.20 \pm 0.08 \times 10^{-2}$
Kochanek et al. (2001)	-23.43 ± 0.05	1.09 ± 0.06	$1.16 \pm 0.1 \times 10^{-2}$
This paper	-23.36 ± 0.02	0.93 ± 0.04	$1.16 \pm 0.17 \times 10^{-2}$

magnitudes, noting the small offset of $\Delta_{\text{cal}}^{\text{Kron}} + \Delta_{\text{Kron}} - \Delta_{\text{conv}} = 0.08\text{–}0.15$ required to convert to total magnitudes and correct for the convolving effect of measurement errors.

The parameters of the STY Schechter function fits shown in Fig. 13 are listed in the first row of Table 1. The subsequent rows illustrate how the best-fitting parameters change when the cosmological model is varied and the evolutionary correction is included or excluded. The *M** values are approximately 0.14 mag fainter for the $\Omega_0 = 1$ case than for our standard $\Omega_0 = 0.3$, $\Lambda_0 = 0.7$ cosmology. This shift is largely a result of the difference in distance moduli between the two cosmologies at the median redshift of the survey. This, and the difference in the volume–redshift relation, cause ϕ_* to change in order to preserve the same galaxy number counts.

Fig. 15 compares our estimates of the K_S-band luminosity function for our standard $\Omega_0 = 0.3$, $\Lambda_0 = 0.7$ cosmology, with the estimates of Mobasher et al. (1993), Glazebrook et al. (1995), Gardner et al. (1997), Szokoly et al. (1998), Loveday (2000) and Kochanek et al. (2001). In general, these authors assumed different cosmological models when analysing their data. We have therefore modified the estimates from each survey. First, we apply a shift in magnitude reflecting the difference in distance moduli, at the median redshift, between the assumed cosmological model and our standard $\Omega_0 = 0.3$, $\Lambda_0 = 0.7$ model. We then apply a shift in the number density so as to keep fixed the surface density of galaxies per square degree at the survey magnitude limit. In the case of the Kochanek et al. (2001) luminosity function we have shifted the data points brightwards by 0.05 mag to account for the mean difference between the 2MASS isophotal magnitudes used by Kochanek et al. (2001) and the Kron magnitudes that we have adopted. Schechter function parameters scaled and adjusted in this manner are given for each survey in Table 3. Note that because of the correlations between the Schechter function parameters it is better to judge the agreement between the different estimates by a reference to Fig. 15 rather than by the parameter values in Table 3. Our new estimate of the K_S-band luminosity function is in excellent agreement with the independent estimates, and has the smallest statistical errors at all magnitudes brighter than $M_{K_S} - 5\log h = -22$. For very faint magnitudes, from -20 to -16, the sparsely sampled survey of Loveday (2000) has smaller statistical errors. Note that many previous analyses of the *K*-band luminosity function ignored the contribution of large-scale structure to the error in Φ_*, and so the errors in Table 3 are likely to be underestimated.

Also shown on the lower panel of Fig. 15 is an estimate of the *K*-band luminosity function inferred from the Sloan Digital Sky Survey (SDSS) near-infrared, *z**-band luminosity function of Blanton et al. (2001). To convert from *z** (AB system) to the standard *K* we have simply subtracted 2.12 mag from the SDSS *z** magnitudes. This offset consists of a contribution of 0.51 mag to convert from AB magnitudes to the standard Vega system, and a mean *z**–K_S colour of 1.61, which we find is typical of the model spectra discussed in Section 3 that match our observed $b_J - K_S$ colours. As has been noted by Wright (2001) the luminosity function inferred from the SDSS data is offset compared to our estimate. One suggestion put forward by Wright (2001) is that the 2MASS magnitudes could be systematically too faint. The systematic error would have to amount to 0.5 mag to reconcile the luminosity density inferred from the SDSS data with that which we infer from the 2MASS-2dFGRS catalogue. Such an error is comprehensively excluded by the very small offset that was found in Section 2.3 between the 2MASS Kron magnitudes and the data of Loveday (2000). Also, a direct galaxy-by-galaxy comparison of the *z**–*J* and *z**–K_S colours computed using the SDSS Petrosian and the 2MASS Kron magnitudes produced galaxy colours in good accord with expectations based on model spectra (Ivezic, Blanton & Loveday, private communication). Finally, we note that a good match to our estimate of the K_S-band luminosity function cannot be achieved by simply moving the SDDS curve in Fig. 15 horizontally. If slid by 0.5 mag to match the luminosity density then it falls well below our estimate at bright magnitudes. However if the SDSS curve is moved vertically, by a factor of 1.6, then the two estimates come into reasonable agreement at all magnitudes. Thus, the most likely explanation of the difference between the SDSS and 2MASS–2dFGRS luminosity functions is the uncertainty in the overall normalization induced by large-scale density fluctuations. It is to be hoped that as the sky coverage of the SDSS and 2MASS–2dFGRS surveys increases this discrepancy will be reduced.

5.2 Colour distributions

Since our combined 2MASS–2dFGRS catalogue includes b_J-band and infrared magnitudes, it is also possible to estimate the b_J-band optical luminosity function and the optical/infrared bivariate luminosity function. We do not present the b_J-band optical luminosity function here as estimates from the 2dFGRS are discussed in detail in Norberg et al. (in preparation) and
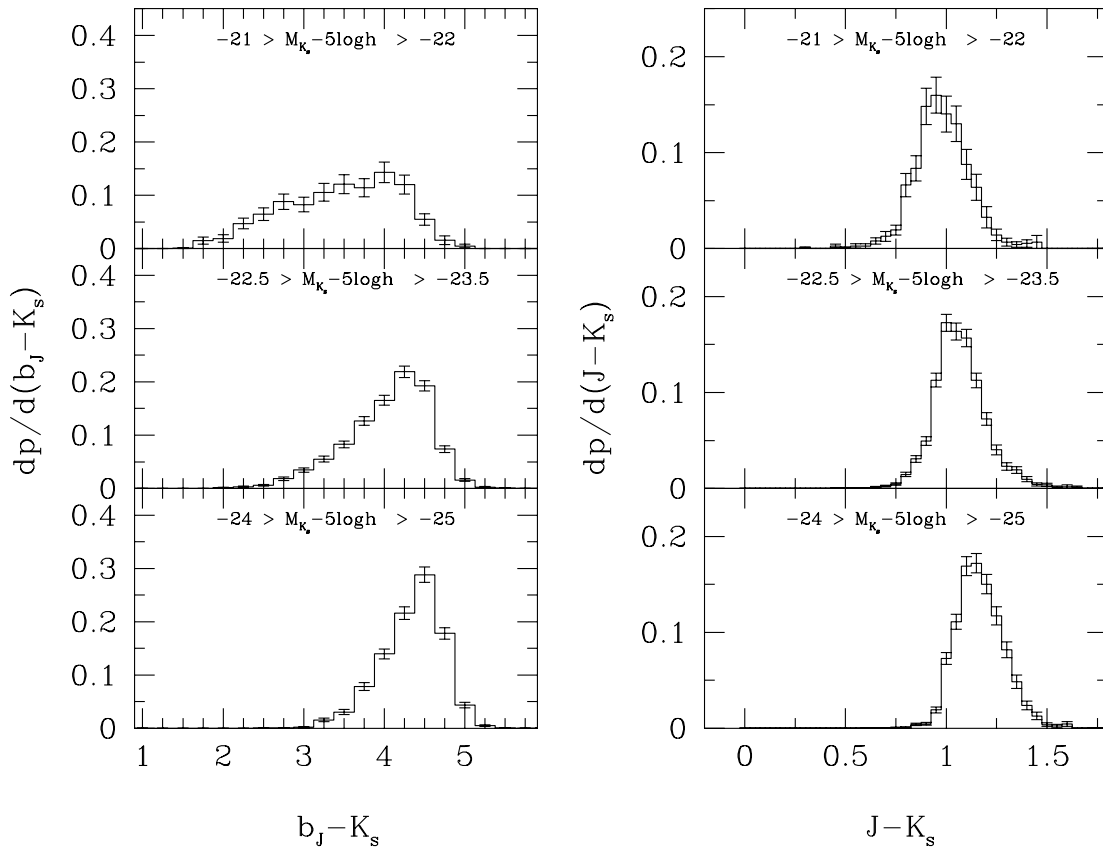
Figure 16. The distribution of rest-frame $b_J - K_S$ (left) and $J - K_S$ (right) colours in three bins of K_S absolute magnitude, computed using our default set of k+e corrections.

decomposed into luminosity functions of different spectral types in Folkes et al. (1999) and Madgwick, Lahav & Taylor (2001). Instead, we present the bivariate b_J/K_S and J/K_S luminosity functions in Fig. 16, in the form of the rest-frame $b_J - K_S$ and $J - K_S$ colour distributions, split by the K_S-band absolute magnitude. Results are shown for just our default set of k+e corrections, but the colour distributions are extremely insensitive to this choice and to whether evolutionary corrections are ignored or included. The shape of the $b_J - K_S$ colour distribution varies systematically with the K_S-band luminosity. At fainter magnitudes there is an increasingly large population of bluer, star-forming galaxies. The star formation rate has less effect on the infrared $J - K_S$ colours. Here, the shape of the $J - K_S$ colour distribution varies little with luminosity, but the position of the peak moves gradually redder with increasing luminosity. Colour distributions such as these are sensitive to both the distribution of stellar age and the metallicity, and therefore provide important constraints on models of galaxy formation (for example, see Cole et al. 2000).

5.3 Spectral type distribution

Another interesting issue that we can address with our data is the distribution of spectral types in the 2MASS catalogue. For this, we make use of the spectral information in the 2dF galaxies extracted by a principal component analysis (Folkes et al. 1999). Specifically, we use the new continuous variable introduced by Madgwick et al. (2001) which is defined by a linear combination of the first two principal component projections, $\eta \equiv 0.44pc_1 - pc_2$. This variable was chosen to be robust to instrumental uncertainties whilst, at the same time, preserving physical information about the
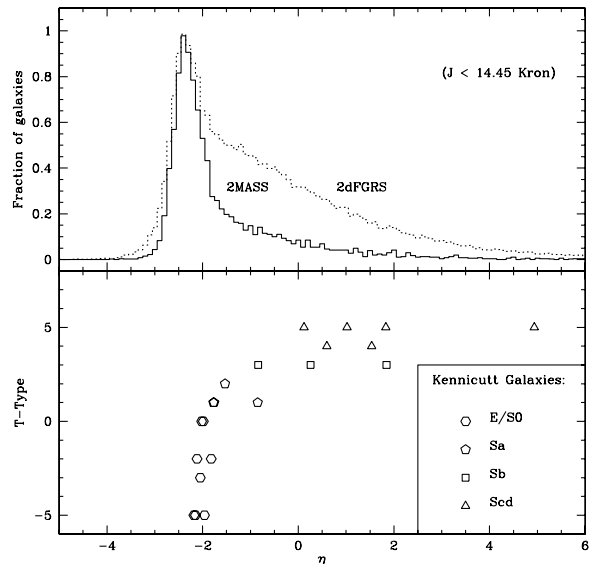

Figure 17. The distribution of the spectral type parameter, η, in the full 2dFGRS and our matched 2MASS catalogue (upper panel). The lower panel uses a sample of galaxies from Kennicutt (1992) to show how η is correlated with morphological type.

galaxy. The dominant influence on the η parameter is the relative strength of absorption and emission lines ($\eta < 0$ implies less than average emission-line strength while $\eta > 0$ implies stronger than average emission-line strength). A more detailed description will be presented by Madgwick et al. (in preparation).

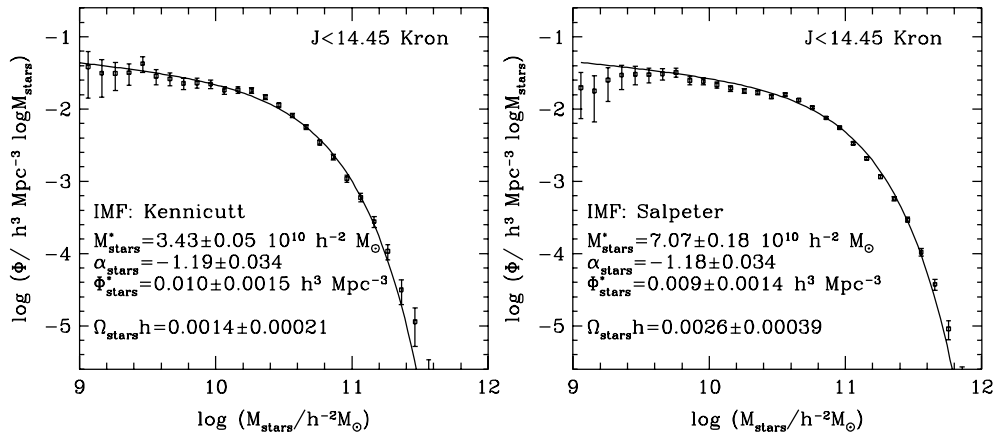We can now gain insight into the population mix of our 2MASS

Figure 18. SWML estimates of the stellar mass function (open symbols with error bars) and STY Schechter function estimates (lines). The parameter and error estimates of the Schechter function fits are given in the legends. The left-hand panel is for a Kennicutt IMF with recycled fraction $R = 0.42$ and the right-hand panel for a Salpeter IMF with $R = 0.28$.

sample by simply creating a histogram of the η values for the corresponding 2MASS–2dFGRS matched galaxies with $J < 14.45$ (Kron). We plot this in Fig. 17 where we also show the data for the entire 2dFGRS sample as comparison. Also shown in Fig. 17 (bottom panel) is the morphology–η relation derived from a sample of galaxy spectra from the Kennicutt Atlas (Kennicutt 1992).

It can be clearly seen from Fig. 17 that the predominant population in the 2MASS sample has $\eta < -2$. By contrasting this with values of η obtained from the spectra of galaxies with known morphological type (Kennicutt 1992), we can see that this corresponds to galaxies of E/S0 morphologies. More precisely, the fraction of galaxies in our matched sample with spectral types corresponding to E/S0 morphologies is 62 per cent (compared with ~35 per cent in the full 2dFGRS). Sa–Sb galaxies make up a further 22 per cent and the remaining 16 per cent are galaxies of later morphological types.

5.4 The galaxy stellar mass function

In contrast to optical light, near-infrared luminosities are relatively insensitive to the presence of young stars and can be more accurately related to the underlying stellar mass. Thus, with relatively few model assumptions, we can derive the distribution of galaxy stellar masses. The integral of this distribution is the total mass density in stars, which can be expressed in units of the critical density as Ω_{stars}. Attempts to estimate this quantity date back to many decades, but even recent estimates such as those by Persic & Salucci (1992), Fukugita, Hogan & Peebles (1998) and Salucci & Pecsic (1999) have very large uncertainties because they are based on the B-band light and require uncertain B-band mass-to-light ratios. The much more accurate estimate that we provide here should prove very useful for a variety of purposes.

To estimate the galaxy stellar mass function, we use the modelling of the stellar populations described in Section 3 to obtain estimates of the present luminosity and stellar mass-to-light ratio for each galaxy in the survey. This is done on a galaxy-by-galaxy basis as described in Section 3. The sample we analyse is defined by the $11 < J < 14.45$ (Kron) apparent magnitude limits. The stellar mass that we estimate for each galaxy is the mass locked up in stars and stellar remnants. This differs from the time integral of the star formation rate because some of the material that

Table 4. The SWML stellar mass functions as plotted in Fig. 18. The units of both ϕ and its uncertainty $\Delta\phi$ are number per $h^{-3}\,\mathrm{Mpc}^3$ per decade of mass.

$\log_{10} M$	Kennicutt $\phi \pm \Delta\phi$	Salpeter $\phi \pm \Delta\phi$
9.06	$(4.24 \pm 2.62) \times 10^{-2}$	$(1.37 \pm 1.05) \times 10^{-2}$
9.16	$(3.42 \pm 1.80) \times 10^{-2}$	$(2.41 \pm 1.35) \times 10^{-2}$
9.26	$(3.01 \pm 1.31) \times 10^{-2}$	$(2.06 \pm 1.13) \times 10^{-2}$
9.36	$(3.33 \pm 1.11) \times 10^{-2}$	$(3.01 \pm 1.13) \times 10^{-2}$
9.46	$(4.21 \pm 1.04) \times 10^{-2}$	$(3.25 \pm 0.92) \times 10^{-2}$
9.56	$(2.75 \pm 0.67) \times 10^{-2}$	$(2.87 \pm 0.67) \times 10^{-2}$
9.66	$(2.70 \pm 0.55) \times 10^{-2}$	$(3.10 \pm 0.56) \times 10^{-2}$
9.76	$(2.31 \pm 0.42) \times 10^{-2}$	$(3.30 \pm 0.47) \times 10^{-2}$
9.86	$(2.20 \pm 0.35) \times 10^{-2}$	$(2.67 \pm 0.34) \times 10^{-2}$
9.96	$(2.21 \pm 0.31) \times 10^{-2}$	$(2.51 \pm 0.27) \times 10^{-2}$
10.06	$(1.77 \pm 0.23) \times 10^{-2}$	$(2.03 \pm 0.20) \times 10^{-2}$
10.16	$(1.91 \pm 0.20) \times 10^{-2}$	$(1.93 \pm 0.17) \times 10^{-2}$
10.26	$(1.77 \pm 0.16) \times 10^{-2}$	$(1.86 \pm 0.15) \times 10^{-2}$
10.36	$(1.46 \pm 0.12) \times 10^{-2}$	$(1.62 \pm 0.11) \times 10^{-2}$
10.46	$(1.11 \pm 0.08) \times 10^{-2}$	$(1.49 \pm 0.09) \times 10^{-2}$
10.56	$(8.15 \pm 0.61) \times 10^{-3}$	$(1.61 \pm 0.08) \times 10^{-2}$
10.66	$(5.62 \pm 0.43) \times 10^{-3}$	$(1.30 \pm 0.06) \times 10^{-2}$
10.76	$(3.39 \pm 0.29) \times 10^{-3}$	$(1.06 \pm 0.04) \times 10^{-2}$
10.86	$(2.08 \pm 0.20) \times 10^{-3}$	$(7.40 \pm 0.30) \times 10^{-3}$
10.96	$(1.07 \pm 0.12) \times 10^{-3}$	$(5.50 \pm 0.22) \times 10^{-3}$
11.06	$(5.95 \pm 0.82) \times 10^{-4}$	$(3.29 \pm 0.15) \times 10^{-3}$
11.16	$(2.75 \pm 0.49) \times 10^{-4}$	$(2.02 \pm 0.10) \times 10^{-3}$
11.26	$(1.05 \pm 0.26) \times 10^{-4}$	$(1.13 \pm 0.07) \times 10^{-3}$
11.36	$(2.77 \pm 1.11) \times 10^{-5}$	$(5.56 \pm 0.40) \times 10^{-4}$
11.46	$(9.51 \pm 5.65) \times 10^{-6}$	$(2.90 \pm 0.26) \times 10^{-4}$
11.56	$(2.05 \pm 2.38) \times 10^{-6}$	$(9.87 \pm 1.26) \times 10^{-5}$
11.66	$(6.87 \pm 13.6) \times 10^{-7}$	$(3.73 \pm 0.66) \times 10^{-5}$
		$(8.46 \pm 2.58) \times 10^{-6}$
		$(2.22 \pm 1.20) \times 10^{-6}$

goes into forming massive stars is returned to the interstellar medium via winds and supernovae. For a given IMF, this recycled fraction, R, can be estimated reasonably accurately from stellar evolution theory. Here, we adopt the values $R = 0.42$ and 0.28 for the Kennicutt (1983) and Salpeter (1955) IMFs respectively, as described in section 5.2 of Cole et al. (2000) who made use of the models of Renzini & Voli (1981) and Woosley & Weaver (1995). Hence, the stellar masses we choose to estimate are $(1 - R)$ times the time integral of the star formation rate to the present day. Note
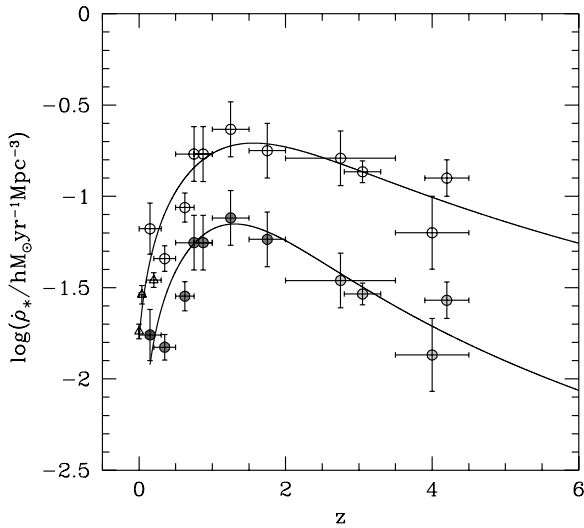
Figure 19. Observational estimates of the star formation history of the Universe. The points with error bars show estimates of the mean star formation rate per unit volume at various redshifts (see Steidel et al. 1999 and references therein). The solid symbols are the star formation rates implied if there is no absorption by dust. The open symbols show estimates corrected for dust absorption using a Calzetti (1999) extinction law with a mean $E(B - V) = 0.15$ (Steidel et al. 1999). In both cases an $\Omega_0 = 0.3$, $\Lambda_0 = 0.7$ cosmology has been used to calculate the volume as a function of redshift and a Salpeter IMF to convert luminosity to star formation rate. The smooth curves are the fits we use when we integrate over time to estimate the total mass density of stars formed at the present.

that the IMFs we consider assume that only stars with mass greater than $0.1\,M_\odot$ ever form and so we are not accounting for any mass that may be locked up in the form of brown dwarfs.

Our results are presented in Fig. 18 which shows both SWML and Schechter function estimates of the present-day galaxy stellar mass function for two choices of IMF. The SWML estimates are tabulated in Table 4. Just as for the luminosity functions, the stellar mass function is well described by the Schechter functional form. Integrating over these Schechter functions to determine the total stellar mass gives $\Omega_{\text{stars}} h = (1.4 \pm 0.21) \times 10^{-3}$ for the Kennicutt IMF and $\Omega_{\text{stars}} h = (2.6 \pm 0.39) \times 10^{-3}$ for the Salpeter IMF. Note that the integral converges rapidly at both limits and, in particular, the contribution to Ω_{stars} from objects with $M_{\text{stars}} < 10^9\,h^{-2}\,M_\odot$ is negligible. We find that these values vary by less than the quoted errors when we alter the assumed (k+e) − corrections by either ignoring evolution, dust or changing Ω_0. Taken together with our estimates of the K_S-band luminosity density these estimates imply mean stellar mass-to-light ratios of $0.73\,M_\odot/L_\odot$ in the case of the Kennicutt IMF and $1.32\,M_\odot/L_\odot$ for the Salpeter IMF. If we apply the correction we estimated in Section 2.3 to transform 2MASS Kron into total magnitudes, then these estimates and their uncertainties increase to $\Omega_{\text{stars}} h = (1.6 \pm 0.24) \times 10^{-3}$ for the Kennicutt IMF and $\Omega_{\text{stars}} h = (2.9 \pm 0.43) \times 10^{-3}$ for the Salpeter IMF. Both of these estimates are consistent with the value, $\Omega_{\text{stars}} = (3.0 \pm 1.0) \times 10^{-3}$, derived by Sali & Persic (1999) but have fractional statistical errors which are several times smaller. With our method, the uncertainty in Ω_{stars} is clearly dominated by the uncertainty in the IMF. For some purposes, it is not possible to improve upon this without a more precise knowledge of the true IMF – assuming that there is a universal IMF. However, for other applications, such as modelling the star formation history of the universe, it is necessary to assume a specific IMF to convert the

Table 5. Estimates of the present-day mass in stars and stellar remnants obtained by integrating over observational estimates of the star formation history of the Universe. We express this stellar mass density in terms of the critical density and give values of $\Omega_{\text{stars}} h^2$ estimated for different assumed IMFs and dust corrections. All values are for an $\Omega_0 = 0.3$, $\Lambda_0 = 0.7$ cosmology and assume stellar populations of solar metallicity.

Dust extinction	Kennicutt IMF	Salpeter IMF
$E(B - V) = 0.05$	0.80×10^{-3}	1.30×10^{-3}
$E(B - V) = 0.10$	1.17×10^{-3}	1.86×10^{-3}
$E(B - V) = 0.15$	1.63×10^{-3}	2.66×10^{-3}

observational tracers of star formation to star formation rates. Hence, in this case, it is the much smaller statistical errors that are relevant.

It is interesting to compare our values with what is inferred by integrating the observational estimates of the mean star formation history of the Universe. Fig. 19 shows observational estimates for one particular choice of cosmology and IMF, and illustrates how the rates are sensitive to the assumed dust extinction. By fitting a smooth curve through these estimates, we can calculate the mass of stars formed by the present day and how this depends on the IMF and assumed dust extinction. The upper smooth curve shown in Fig. 19 is of the form $\dot{\rho}_* = (a + bz)/[1 + (z/c)^d]\,h\,M_\odot\,\text{yr}^{-1}\,\text{Mpc}^{-3}$, where $(a, b, c, d) = (0.0166, 0.1848, 1.9474, 2.6316)$. The data points uncorrected for dust extinction are fit with $(a, b, c, d) = (0.0, 0.0798, 1.658, 3.105)$. As for our estimates above, we assume that no mass goes into forming brown dwarfs and multiply the star formation rate by $1 - R$, where R is the recycled fraction, so as to form an estimate of the mass locked up in stars. Values of $\Omega_{\text{stars}} h^2$ estimated in this way are listed in Table 5. The values in this table are for an $\Omega_0 = 0.3$, $\Lambda_0 = 0.7$ cosmology, but they are insensitive to this choice. They depend slightly on the assumed metallicity of the stellar population, and would be 10 per cent lower if the half solar, rather than solar metallicity were assumed. Note that the Ω_{stars} values inferred from the star formation history of the Universe scale differently with the assumed Hubble constant than those inferred above from the IR luminosity functions. For $h = 0.7$ our estimates from 2MASS become $\Omega_{\text{stars}} h^2 = (1.12 \pm 0.16) \times 10^{-3}$ for the Kennicutt IMF and $\Omega_{\text{stars}} h^2 = (2.03 \pm 0.30) \times 10^{-3}$ for the Salpeter IMF. Comparison with Table 5 shows that these values are consistent with those inferred from the cosmic star formation history only if the dust correction assumed in the latter is modest, $E(B - V) \approx 0.1$. This value is 50 per cent smaller than the value preferred by Steidel et al. (1999).

6 CONCLUSIONS

The new generation of very large surveys currently underway make it possible to characterize the galaxy population with unprecedented accuracy. In this paper, we have combined two such large surveys, the infrared imaging 2MASS and the 2dF Galaxy Redshift Survey[1] to obtain a complete data set which is more than an order

---

[1] A table containing the positions, 2MASS infrared magnitudes and 2dFGRS redshifts used in this paper, and electronic versions of Tables 2 and 4 are available at http://star-www.dur.ac.uk/n~cole/2dFGRS-2MASS.

of magnitude larger than the previous data sets used for statistical studies of the near-infrared properties of the local galaxy population. We have used this combined catalogue to derive the most precise estimates to date of the galaxy J and K_S-band luminosity functions and of the galaxy stellar mass function.

Characterizing the near-infrared properties of galaxies offers several advantages. First, the near-infrared light is dominated by established, old stellar populations rather than by the recent star formation activity that dominates the blue light. Thus, the J and K-band luminosity functions reflect the integrated star formation history of a galaxy and, as a result, provide particularly important diagnostics of the processes of galaxy formation. For the same reason, the distribution of stellar mass in galaxies –the galaxy stellar mass function– can be derived from the near-infrared luminosities in a relatively straightforward way, with only a weak model dependence. Finally, corrections for dust extinction as well as k-corrections are much smaller in the near-infrared than in the optical.

Because of the size of our sample, our determination of the J- and K_S-band galaxy luminosity functions have, for the most part, smaller statistical errors than the previous estimates. Furthermore, since our sample is infrared selected, our estimates are free from any potential biases that might affect infrared luminosity functions derived from optically selected samples. We find that the J- and K_S-band galaxy luminosity functions are fairly well described by Schechter functions, although there is some evidence for an excess of bright galaxies relative to the best-fitting Schechter functional form. In general, the SWML estimates are a truer representation of the luminosity functions. Our K-band estimates are in overall agreement with most previous determinations, but have smaller statistical errors.

The exception is the K-band luminosity function inferred from the near-infrared SDDS photometry (Blanton et al. 2001). The difference between the K-band luminosity function that we infer from their data and our own estimate is too large to be explained by photometric differences. The difference between the two estimates is better described by a difference of a factor of 1.6 in the overall number density. A similar discrepancy is seen in the b_J-band between the SDSS and 2dFGRS luminosity function estimates (see Norberg et al., in preparation; Blanton et al. 2001). The suspicion is that the uncertainty in the overall normalization of the luminosity functions induced by the large-scale structure within the large, but finite, survey volumes could be to blame. However, the errors that we quote for the 2dFGRS–2MASS luminosity functions already include an estimate of this sampling uncertainty as derived from realistic mock catalogues. A similar exercise for a catalogue with the same area and depth as that of Blanton et al. (2001) indicates that the required overdensity of a factor of 1.6 is unlikely. So probably there is more than one contributory factor at work and the hope is that these will be identified as the surveys progress.

Using our J-band luminosity function, $b_J - K_S$ and $J - K_S$ colours and simple galaxy evolutionary tracks, we have obtained the first estimate of the galactic stellar mass function derived directly from the near-infrared data. We find that this mass function is also fairly well described by a Schechter form. An integral over the stellar mass function gives Ω_{stars}, the universal mass density locked up in luminous stars and stellar remnants, expressed in terms of the critical density. Ω_{stars} is a key component of the overall inventory of baryons in the Universe. An accurate determination of this quantity is essential for detailed comparisons with other quantities of cosmological interest such as the total baryonic mass, Ω_{baryon}, inferred from big bang nucleosynthesis considerations

(e.g. Burles & Tytler 1998), the cosmic star formation rate (e.g. Steidel et al. 1999), and the cosmic evolution of the gas content of the Universe (Storrie-Lombardi & Wolfe 2000). The statistical uncertainty in our estimate of Ω_{stars} is about 15 per cent, several times smaller than the best previous determination by Selucci & Persic (1999). In fact, the errors in Ω_{stars} are dominated by systematic uncertainties associated with the choice of stellar IMF in the galaxy evolution model. A Kennicutt IMF gives $\Omega_{stars} h = (1.6 \pm 0.24) \times 10^{-3}$ while a Salpeter IMF gives $\Omega_{stars} h = (2.9 \pm 0.43) \times 10^{-3}$. For $h = 0.7$, these values correspond to less than 11 per cent of the baryonic mass inferred from the big bang nucleosynthesis (Burles et al. 1999). Our values of Ω_{stars} today are only consistent with recent determinations of the integrated cosmic star formation if the correction for dust extinction is modest.

REFERENCES

Allen C. W., 1973, Astrophysical Quantities, 3rd edn. Athlone Press, London
Blanton M. R. et al., 2001, AJ, 121,2358
Bruzual A. G., Charlot S., 1993, ApJ, 405, 538
Burles S., Tytler D., 1998, ApJ, 507, 732
Burles S., Nollet K. M., Truran J. N., Turner M. S., 1999, Phys. Rev. Lett., 82, 4176
Calzetti D., 1999, Ap&SS, 266, 243
Carpenter J. M., 2001, AJ, 324, 825
Cole S., Lacey C. G., Baugh C. M., Frenk C. S., 2000, MNRAS, 319, 168
Cross N. et al., 2001, MNRAS, in press (astro-ph/0012165)
Efstathiou G., Ellis R. S., Peterson B. A., 1988, MNRAS, 232, 431
Evrard A. E., 1999, in Banday T., Sheth R., da Costa L. N., eds, in Proc. MPA-ESO Cosmology Conf. From Recombination to Garching. ESO Publications, Garching bei, München, p. 249
Ferrara A., Bianchi S., Cimatti A., Giovanardi C., 1999, ApJS, 123, 423
Folkes S. et al., 1999, MNRAS, 308, 459
Fukugita M., Hogan C. J., Peebles P. J. E., 1998, ApJ, 503, 518

Gardner J. P., Sharples R. M., Carrasco B. E., Frenk C. S., 1996, MNRAS, 282, 1

Gardner J. P., Sharples R. M., Frenk C. S., Carrasco B. E., 1997, ApJ, 480, 99

Glazebrook K., Peacock J. A., Collins C. A., Miller L., 1994, MNRAS, 266, 65

Glazebrook K., Peacock J. A., Miller L., Collins C. A., 1995, MNRAS, 275, 169

Jarrett T. H., Chester T., Cutri R., Schneider S., Skrutskie M., 2000, ApJ, 119, 2498

Johnson H. L., 1966, ARA&A, 4, 193

Kennicutt R. C., 1983, ApJ, 272, 54

Kennicutt R. C., 1992, ApJS, 79, 255

Kochanek C. S. et al., 2001, ApJ, in press (astro-ph/0011456)

Kron R. G., 1980, ApJS, 43, 305

Loveday J., 2000, MNRAS, 312, 517

Maddox S. J., Efstathiou G., Sutherland W. J., Loveday J., 1990a, MNRAS, 243, 692

Maddox S. J., Efstathiou G., Sutherland W. J., 1990b, MNRAS, 246, 433

Maddox S. J., Sutherland W. J., Efstathiou G., Loveday J., Peterson B. A., 1990c, MNRAS, 247, 1P

Maddox S. J., Efstathiou G., Sutherland W. J., Loveday J., 1996, MNRAS, 283, 1227

Madgwick D., Lahav O., Taylor K., 2001, ESO Astrophysics Symp. Springer-Verlag, in press (astro-ph/0010307)

Metcalfe N., Fong R., Shanks T., 1995, MNRAS, 274, 769

Mobasher B., Sharples R. M., Ellis R. S., 1993, MNRAS, 263, 560

Persic M., Salucci P., 1999, MNRAS, 309, 923P

Phillipps S., Davies J., Disney M., 1990, MNRAS, 242, 235

Renzini A., Voli M., 1981, A&A, 94, 175

Salpeter E. E., 1955, ApJ, 121, 61

Salucci P., Persic M., 1999, MNRAS, 309, 923

Sandage A., Tammann G. A., Yahil A., 1978, ApJ, 232, 352

Shanks T., 1990, in Mattilla K., ed., Galactic and Extragalactic Background Radiation. Reidel, Dordrecht, p. 269

Steidel C. C., Adelberger K. L., Giavalisco M., Dickinson M., Pettini M., 1999, ApJ, 519, 1

Storrie-Lombardi L., Wolfe A., 2000, ApJ, 543, 552 (astro-ph/0006044)

Szokoly G. P., Subbarao M. U., Connolly A. J., Mobasher B., 1998, ApJ, 492, 452

Woosley S. E., Weaver T. A., 1995, ApJS, 101, 181

Wright E. L., 2001, ApJ, submitted (astro-ph/0102053)

This paper has been typeset from a TEX/LATEX file prepared by the author.